Sulfur inventory of the young lunar mantle constrained by experimental sulfide saturation of Chang'e-5 mare basalts and a new sulfur solubility model for silicate melts in equilibrium with sulfides of variable metal–sulfur ratio

Dian Ji [*] ![ORCID], Rajdeep Dasgupta ![ORCID]

Department of Earth, Environmental and Planetary Sciences, Rice University, 6100 Main Street, MS 126, Houston, TX 77005, USA

ARTICLE INFO

ABSTRACT

Assessing whether the lunar mantle retains sulfide, through episodes of magmatism, is important in tracking the origin and evolution of sulfur and other volatile and chalcophile elements on the Moon. To determine sulfur concentrations at sulfide saturation (SCSS) in the mantle conditions of young Chang'e-5 (CE-5) mare basalts, we conducted experiments with three possible CE-5 parental melt compositions and Fe $\pm$ Ni-S sulfide at 1.0–3.0 GPa and 1250–1550 °C. We doped excess Fe metal in a subset of experiments in order to generate sulfide of various metal/sulfur molar ratio (M/S; 1.0–2.1), and thus investigate the effect of sulfide composition on SCSS under different oxygen fugacities (fO_2s). Our experimental results indicate that SCSS is sensitive to temperature, pressure, silicate melt, sulfide compositions, and fO_2. Using our new and literature data, we developed a new thermodynamic SCSS model and utilized the model to calculate the SCSS for scenarios that the CE-5 parental melt is in equilibrium with pure FeS, high Fe/S ratio sulfide, as well as high M/S Ni-bearing sulfide. All results suggest predictive SCSS values are higher than the S concentration in CE-5 parental magma, indicating the CE-5 mantle residue was likely sulfide-absent, unless an extremely S-poor and Ni-rich, Fe-alloy was the chief S-bearing accessory phase. We further reconstruct the S abundance in the CE-5 mantle source. Compared with the mantle of Apollo mare basalts, the $\sim$ 2 Gyrs lunar mantle has much lower S abundances, suggesting sulfur extraction by mantle melting over the magmatic history of the Moon, or S distribution heterogeneity in the lunar interior.

1. Introduction

The volatile abundance in the lunar mantle informs the formation and evolution of the Earth-Moon system. The early analyses of the Apollo samples proposed a volatile depleted Moon (e.g., Ringwood and Kesson, 1977; Taylor et al., 2006), consistent with the giant impact theory for the formation of the Moon (e.g., Canup and Asphaug, 2001; Hartmann and Davis, 1975). However, recent studies of lunar melt inclusions and volcanic glasses suggested that the lunar mantle may have greater budget of highly volatile elements than previously thought, with some budgets (e.g., water and sulfur) even overlapping with the Earth's upper mantle (Hauri et al., 2015; McDonough and Sun, 1995; Wang and Becker, 2013), requiring volatiles to survive the giant impact or replenishment by late veneers. Among all major volatile elements, sulfur (S) is both volatile and chalcophile, which allows it to provide additional

clues about the evolution of the lunar mantle (e.g., Day, 2018; Brenan et al., 2019; Saal and Hauri, 2021). The lunar mantle is expected to store S in the form of accessory sulfide (e.g., Ding et al., 2018; Dasgupta et al., 2022). As a volatile, incompatible element, S is concentrated in the silicate melt during mantle melting and related magmatic processes (Callegaro et al., 2020; Johnson et al., 2024; Jugo et al., 2005; O'Neill and Mavrogenes, 2002). At the onset of melting, the basaltic lunar melt is expected to be sulfide saturated, with S content set by the sulfur concentrations at sulfide saturation (SCSS; e.g., Haughton et al., 1974; Steenstra et al., 2020b). However, depending on the lunar mantle S content, the relevant SCSS, and the conditions of mantle melting, the fate of the accessory sulfide phase may vary (e.g., Ding and Dasgupta, 2017; Dasgupta et al., 2022). Constraints on the SCSS of lunar-relevant melt compositions and melting conditions can help determining the lunar interior sulfur cycle. However, such constraints remain limited.

Recently returned Chang'e-5 (CE-5) samples are unique for their young age (~2.03 Ga; Li et al., 2021; Che et al., 2021), casting new light on the late-stage evolution of volatiles in the lunar mantle. A previous study showed that the mantle source of CE-5 basalts has much lower water abundance (1–6 ppm) than the source of Apollo samples and lunar meteorites, which may suggest the continued magmatic activities in the mantle (Hu et al., 2021). Researchers reported the S abundances and isotopic compositions of CE-5 mare basalt (Liu et al., 2022; Wang et al., 2024b), suggesting the CE-5 mare basalt have experienced ~ 40 % of S loss by equilibrium degassing, and the S concentrations before degassing is ~ 600 ± 300 ppm (Liu et al., 2022), much lower than the SCSS determined by previous high-FeO* lunar mare basalt experiments (Ding et al., 2018; Steenstra et al., 2018). However, Brenan et al. (2019) suggested that under low oxygen fugacity (fO_2) associated with the lunar mantle [~one to two log units below iron-wüstite (IW) buffer; e.g., Wadhwa, 2008; Ji and Dygert, 2023; Zhang et al., 2024], the existence of S-poor, Fe-rich sulfide may lead to much lower SCSS, as low as a few hundred ppm for the parental melt of Apollo samples. Therefore, the mantle residue of lunar mare volcanic suites could be saturated with sulfide. Yet, the possibility that young CE-5 lunar basalts could be in equilibrium with high metal-to-sulfur molar ratio (M/S) sulfides, has never been systematically tested under the proposed conditions of petrogenesis (e.g., Haupt et al., 2023; Su et al., 2022; Luo et al., 2023; Wang et al., 2024a). One reason may be the lack of SCSS models that can be applied to lunar-relevant sulfide systems at low fO_2.

Previous studies developed the predictive SCSS models for terrestrial melts (e.g., Blanchard et al., 2021; Fortin et al., 2015; Liu et al., 2021; Smythe et al., 2017) and also for high-FeO* (FeO* denotes that all Fe is reported as $Fe^{2+}O$) lunar melt compositions (e.g., Ding et al., 2018; Steenstra et al., 2018). However, most previous lunar and terrestrial SCSS models did not consider the effect of fO_2 and its role on the sulfide composition. Therefore, the relation between fO_2, sulfide composition, and SCSS is still unconstrained. Although few studies conducted S solubility experiments at lunar-relevant fO_2, they either do not report accurate sulfide compositions (e.g., Mavrogenes and O'Neill, 1999; Holzheid and Grove, 2002), or the analytical uncertainties of SCSS are significant (e.g., Holzheid and Lodders, 2001). Brenan et al. (2019) conducted a series of experiments with Fe capsule to generate the sulfide with M/S as high as ~ 6.0. They applied a two component (Fe-FeS) asymmetric mixing model (Thompson Jr, 1967) to calculate the activity of FeS in sulfide, and the model from Ding et al. (2018) to calculate the SCSS. However, there is a gap in fO_2 and M/S ratio between the experiments in Brenan et al. (2019) that generated high M/S ratio sulfides (logfO_2 < IW–0.8; M/S > 3.5) and previous studies focused on lunar and terrestrial environment (logfO_2 > IW; M/S ≈ 1). In addition, the model is difficult to apply to all the lunar sulfides because some are reported to contain Ni at weight-percent levels (e.g., Papike et al., 2011). The mass balance calculation further suggested the lunar sulfide may hold up to ~ 12 wt% of Ni, which can reduce SCSS by 5 – 20 % (Brenan et al., 2019). Moreover, neglecting the role of Cu-rich sulfides may limit their application under terrestrial conditions (Smythe et al., 2017). Considering the limited number of experiments reported by Brenan et al. (2019), which may not be representative of all lunar sulfide and all petrogenetic conditions, we did a series of sulfide saturation experiments in this study. We simulated parental melt of young CE-5 basalt, coexisting with pure FeS or high M/S sulfides, to expand the experimental database under low fO_2s and develop an SCSS model for equilibrium sulfide with variable M/S ratios. We applied our model to possible CE-5 parental melts, which indicated the mantle residue was likely sulfide-absent, unless the chief S-bearing phase was extremely Ni-enriched with a high M/S ratio (e.g., M/S = 6 with ~ 20 wt% Ni). Our calculations suggest that the S content of the CE-5 mantle source may be as much as an order of magnitude depleted compared to the mantle source of Apollo low-Ti and high-Ti mare basalts, reflecting continuous or intermittent depletion of mantle S via melt extraction if the lunar mantle is homogeneous in sulfur budget.

2. Methods

2.1. Experimental starting materials

Three different starting materials, based on the recent estimates of CE-5 parental melt compositions, were used in this study (Haupt et al., 2023; Luo et al., 2023; Su et al., 2022) (Table 1), for the purpose of testing how the SCSS may vary with different proposed petrogenesis. The parental melts in Haupt et al. (2023) and Luo et al. (2023) are whole rock compositions from Che et al. (2021) and Tian et al. (2021) respectively, assuming the most primitive CE-5 basalts are generated by mantle melting directly, while the parental melt in Su et al. (2022) is modeled using PETROLOG program (Danyushevsky and Plechov, 2011) with the hypothesis that the CE-5 basalts are products of extensive fractional crystallization after prior mantle melting.

All starting materials were prepared by grinding reagent-grade oxide and carbonate powders into homogeneous mixtures under ethanol for at least two hours, and then drying overnight at room temperature. To minimize absorbed water, prior to mixing, the reagent grade SiO_2, TiO_2, Al_2O_3, and MgO were fired overnight at 1000 ℃, Fe_2O_3 at 800 ℃, MnO_2 at 400 ℃, $CaCO_3$ at 250 ℃, and K_2CO_3 and Na_2CO_3 at 110 ℃. We preconditioned each mixture in a 1000 ℃ CO-CO_2 gas mixing furnace to decarbonate the powder and reduce the mixture to an fO_2 approaching 2-log unit below the fayalite-magnetite-quartz buffer (~FMQ–2). Three experiments were performed at 1.5 GPa, 1600 ℃ for 2 h for obtaining glasses and for determining the actual compositions of synthetic starting mixes before doping sulfides and metals. The experimental products contained only quenched glass, and the results of analysis are reported in Table 1. Synthetic sulfides and metals were then added to the mixture (Table 2), ground thoroughly again, and stored in a desiccator.

2.2. Experimental procedure and conditions

Twenty-one experiments were conducted at the Experimental Petrology Laboratory of Rice University using an end-loaded piston-cylinder apparatus at 1.0–3.0 GPa and 1200–1550 ℃ (Table 2). All experiments employed graphite capsules with ~ 4.5 mm height and ~ 1 mm wall thickness with ~ 1.5 mm thickness of graphite cap. The experimental assemblies comprised cylindrical sleeves of $BaCO_3$ pressure media of 12.7 mm outer diameter, crushable internal MgO spacers, straight-walled graphite furnaces, and graphite capsules containing the starting mixes. The friable assemblies were contained in Pb foils, which also served as lubricant during high *P-T* experiments. The *P-T* calibration of this assembly was provided in Tsuno and Dasgupta (2011), with uncertainties of ± 0.1 GPa and ~± 12 ℃.

All experiments were pressurized cold to target pressures and then heated to 700–800 ℃, where the experiments were sintered for 2–22 h to minimize the porosity in the capsules and diminish the leakage of sulfides during the experiments. The temperature was then raised to the target temperature. The ramp rate was 100 ℃/min. The durations of experiments were varied from 5 to 72h (Table 2). The experimental temperatures were controlled and monitored using calibrated Type-C thermocouples, and terminated by cutting power to the heater and slowly decompressed. The recovered capsules were mounted in Petropoxy and polished down to 0.1 µm using alumina slurry on a velvet cloth.

2.3. Analytical techniques

Major element concentrations of the experimental phases were analyzed using a JEOL JXA-8530F Hyperprobe at Rice University. We employed a 30 µm spot size with a 50nA beam current to analyze quenched silicate melt, a 20 µm spot size with a 20nA current to analyze sulfide-rich and metallic melt and a focused spot size with a 20nA current to analyze minerals. Analyses are conducted at an accelerating voltage of 15 keV. All phases use chromite as the standard for Cr

Table 1

The parental magma compositions of CE-5 mare basalt from literature and corresponding starting compositions used in this study.

	Target	Synthetic		Target	Synthetic		Target	Synthetic	
	Su et al. (2022)	SS0-2	1σ[b]	Haupt et al. (2023)	HS0-1	1σ[b]	Luo et al. (2023)	LS0-1	1σ[b]
n[a]		20			20			26	
SiO_2	43.68	43.27	0.58	40.6	40.34	0.27	42.43	41.81	0.27
TiO_2	3.08	2.92	0.08	5.7	5.50	0.11	3.13	3.04	0.12
Al_2O_3	6.86	6.89	0.08	11	11.65	0.08	11.98	12.00	0.08
Cr_2O_3	0.64	0.59	0.04	0.37	0.32	0.01	0.3	0.26	0.02
FeO*[c]	19.38	19.10	0.83	24.5	23.62	0.24	19.76	19.66	0.20
MnO	0.23	0.20	0.01	0.29	0.27	0.02	0.26	0.26	0.02
MgO	14	14.23	0.43	4.51	4.73	0.09	9.71	10.05	0.10
CaO	11.2	11.63	0.13	11.7	12.07	0.08	10.7	11.36	0.09
Na_2O	0.2	0.21	0.04	0.38	0.31	0.02	0.53	0.45	0.02
K_2O	0.74	0.70	0.21	0.11	0.08	0.01	0.04	0.04	0.01
P_2O_5	–	0.00	0.00	0.19	0.17	0.00	0.2	0.17	0.01
Total		99.73			99.04			99.10	

[a] Number of EPMA spot analyses averaged.

[b] The 1 sigma uncertainty of analyses.

[c] FeO* denotes that all Fe is reported as $Fe^{2+}O$.

Table 2

Experimental conditions and products.

Experiment#	P (GPa)	T (°C)	Duration at target condition (h)	Sinter T (°C)	Sinter duration (h)	Starting material	Run Product[a]	fO_2 (ΔIW)[b]	SCSS (ppm)[c]
B671	1.5	1500	15	800	8	80 wt% SS0-2 + 20 wt% FeS	Sulfide + Melt	–	5274
B629	2	1500	8	800	16	80 wt% SS0-2 + 20 wt% FeS	Cpx + Sulfide + Melt	–	4727
B670	2	1550	5	800	2	80 wt% SS0-2 + 20 wt% FeS	Sulfide + Melt	–	5016
B626	2.5	1450	18	800	6	80 wt% SS0-2 + 20 wt% FeS	Cpx + Grt + Sulfide + Melt	–	4683
B619	2.5	1500	6	700	20	80 wt% SS0-2 + 20 wt% FeS	Cpx + Sulfide + Melt	–	4335
G807	2.5	1550	5	800	5	80 wt% SS0-2 + 20 wt% FeS	Cpx + Sulfide + Melt	–	4588
B628	3	1500	18	800	5	80 wt% SS0-2 + 20 wt% FeS	Cpx + Grt + Sulfide + Melt	–	4911
B634	2.5	1500	17	800	6	66.7 wt% SS0-2 + 13.3 wt% FeS + 20 wt% Fe	Ol + Cpx + Sulfide + Metal + Melt	−0.41	3640
B633	2	1500	15	800	7	55.6 wt% SS0-2 + 11.1 wt% FeS + 33.3 wt% Fe	Ol + Sulfide + Metal + Melt	−0.44	3300
B632	2.5	1450	16	800	6	55.6 wt% SS0-2 + 11.1 wt% FeS + 33.3 wt% Fe	Ol + Cpx + Sulfide + Metal + Melt	−0.32	4156
B630	2.5	1500	16	800	5	55.6 wt% SS0-2 + 11.1 wt% FeS + 33.3 wt% Fe	Ol + Cpx + Sulfide + Metal + Melt	−0.24	3382
B653	2	1500	23	800	3	85.5 wt% SS0-2 + 8.5 wt% FeS + 6 wt% Ni_3S_2	Ol + Cpx + Sulfide + Melt	–	2381
B654	2	1500	25	800	17	71.4 wt% SS0-2 + 14.3 wt% FeS + 14.3 wt% Ni	Ol + Sulfide + Melt	–	1260
B663	2	1500	16	800	4	74.6 wt% SS0-2 + 8.5 wt% FeS + 10.9 wt% Fe + 6 wt% Ni_3S_2	Sulfide + Metal + Melt	−0.45	2674
T312[d]	1	1250	48	750	18	98 wt% HS0-1 + 2 wt% FeS	Sulfide + Melt + Fe-Ti oxide[e]	–	4766
B667	1.5	1200	72	800	2.5	88 wt% HS0-1 + 12 wt% FeS	Cpx + Grt + Sulfide + Melt	–	5187
B639[d]	1.5	1250	63	800	8.5	98 wt% HS0-1 + 2 wt% FeS	Cpx + Grt + Sulfide + Melt	–	5535
T313	1	1250	47	750	22	66.7 wt% HS0-1 + 13.3 wt% FeS + 20 wt% Fe	Cpx + Fe-Ti oxide + Sulfide + Metal + Melt	−0.26	4663
B649	1	1350	23	800	5	80 wt% LS0-1 + 20 wt% FeS	Sulfide + Melt	–	3471
B665	1.5	1350	20	800	2	80 wt% LS0-1 + 20 wt% FeS	Cpx + Sulfide + Melt	–	3698
B650	1	1350	24	800	14	66.7 wt% LS0-1 + 13.3 wt% FeS + 20 wt% Fe	Sulfide + Metal + Melt	−0.56	2624

The table was organized by starting mixes of the runs, and then for a given starting composition, we arranged the order by increasing P and then increasing T.

[a] Ol = olivine, Cpx = clinopyroxene, Grt = garnet, Metal = metallic melt, Sulfide = sulfide-rich melt, Melt = quenched silicate melt.

[b] The fO_2 relative to IW buffer was calculated using non-ideal solution model. The details are presented in Supplementary Materials.

[c] SCSS = Average sulfur concentrations at sulfide saturation based on replicate electron microprobe analyses. The data are also listed in Table S1 with analytical uncertainties.

[d] We accidentally added only ~ 2 wt% of sulfide in the starting compositions of these two experiments (Fig. S1A), yet sulfide phase was still present, indicating the systems were sulfide saturated.

[e] In this experiment, the Fe-Ti oxide is only located at the bottom of the capsule and in negligible quantity (less than 1 vol%; Fig. S1A). Therefore, condition of this experiment approaches the liquidus.

analysis, rhodonite for Mn, plagioclase for Na, and rutile for Ti. Analytical standards used for minerals are diopside (Mg and Ca), olivine (Si, Fe, and Ni), almandine (Al), and biotite (K). The analysis of glasses employed Smithsonian standard NMNH-113716–1 for Mg, Ca, Al, and S, Smithsonian standard NMNH-117218–3 for K and P, and olivine for Si and Fe. For metals and sulfides, Fe metal was used for Fe, troilite for S, magnetite for O, Si metal for Si, and Ni metal for Ni. Peak and background counting times for the major elements were typically 10 s and 5 s, respectively. The exceptions are P, S, and Ni in glass with peak counts of 30 s and background counts of 15 s, and O and S in sulfide-rich and metallic melts with peak counts of 20 s and background counts of 10 s. Quenched silicate melts and minerals were applied PRZ (JEOL) matrix correction, and sulfides and metals were quantified using the ZAF matrix correction.

3. Results

3.1. Experimental phase assemblage and texture

The experimental assemblages against the conditions are listed in Table 2, and the typical experimental textures are displayed in Fig. 1. In all experiments, the sulfide blobs coexist with quenched silicate melt. The experiments with initial compositions SS0-2 are conducted at higher pressures and temperatures of 1.5–3.0 GPa and 1450–1550 ℃, and the quenched silicate melts from these experiments show dendritic textures (Fig. 1C), while silicate melts in the rest of the experiments with lower pressures (1.0–1.5 GPa) and temperatures (1200 to 1350 ℃) generally produce homogeneous glasses (Fig. 1A). Sulfides existed in the interstitial spaces of dendritic silicate phases in the melt pool (Fig. 1D). Likewise, some exsolved submicron sulfides were observed in the quenched glass (Fig. 1A). We considered them as the products of quenching (Boujibar et al., 2014; Ding et al., 2014). For experiments with an additional Fe metal component, immiscible metal blobs coexisted with sulfide melts (Fig. 1B).

Three experiments with added Ni show skeletal textures in sulfides (Fig. S1). Two experiments doped with additional Ni metal (B654) and Ni_2S_3 + Fe metal (B663), exhibited immiscible metallic melts associated with the sulfide-rich melt blob (Figs. S1C and S1D). We treated skeletal Ni-enriched metals in B654 as part of sulfide because their irregular shape suggests that they were formed during quenching. Therefore, we applied a defocused beam to analyze the average sulfide composition (Fig. S1C). As for B663, however, we observed immiscible Fe-enriched metallic melt blobs with circular boundaries included in the sulfide-rich melt (Fig. S1D). Therefore, we consider components other than Fe-rich metal blobs as sulfide phase and analyze them with a 20 μm beam.

In addition to the immiscible sulfide-rich and metallic melt, various silicate minerals and oxides also were present in the experiments. For experiments with initial composition SS0-2, except three super-liquidus experiments (B663, B670, and B671), all FeS-added experiments produced clinopyroxene, while two experiments at higher pressures (B626 and B628) generated garnet. For experiments with additional metals and/or Ni_2S_3, olivine appeared in the phase assemblages (e.g., Fig. 1B; Table 2). Experiments with the composition HS0-1 produced Fe-Ti oxide
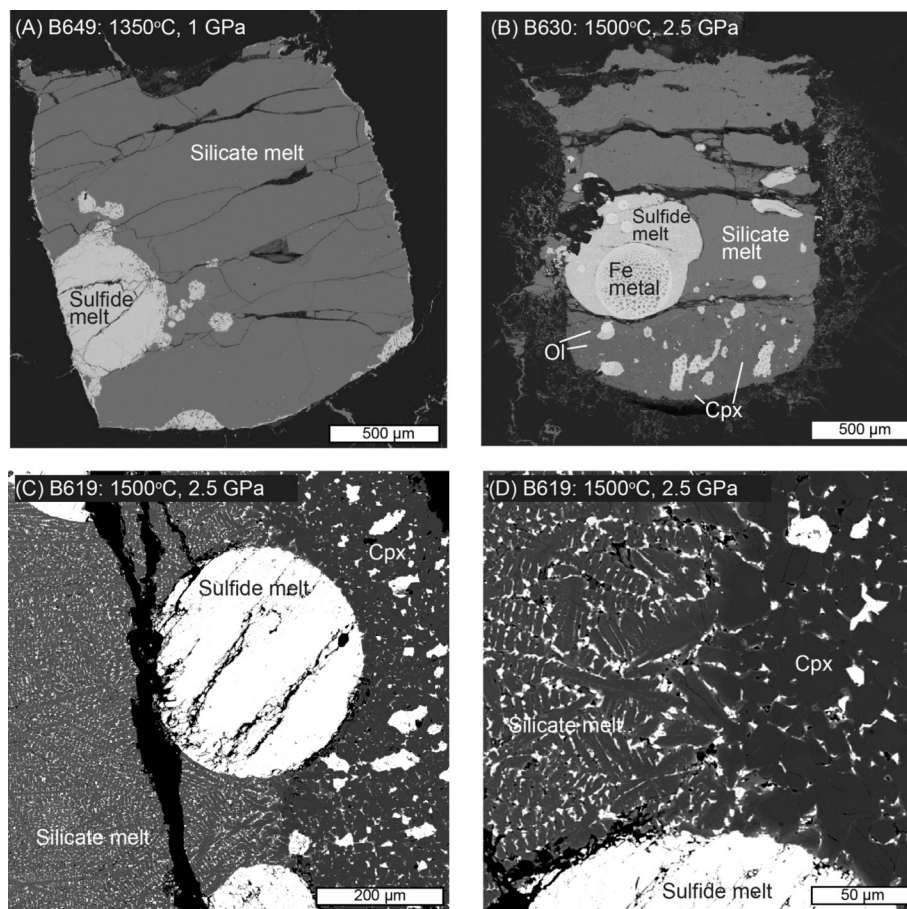
Fig. 1. Representative backscattered electron (BSE) images of the experimental products. (A) An overview of experiment B649 showing quenched silicate glass coexisting with pure FeS. (B) An overview of experiment B630 exhibiting the quenched silicate melt, S-poor sulfide and immiscible Fe-rich metal. Crystallized minerals are clinopyroxene and olivine. (C) The sulfide bleb, and (D) the boundary of quenched silicate melt and clinopyroxene in B619. The dendritic texture of quenched silicate melt can be observed clearly.

and clinopyroxene at 1 GPa and clinopyroxene and garnet at 1.5 GPa and 1200–1250 °C. Only one sub-liquidus experiment with the starting composition LS0-1 produced clinopyroxene at 1.5 GPa and 1350 °C (Table 2).

3.2. Sulfide-rich melt and silicate melt compositions

The compositions of silicate melts, sulfide melts, and metallic melts are listed in Table S1. Six out of our 21 experiments are near- (T312) or super-liquidus (B663, B670, B671, B649, and B650; Table 2), and the compositions of silicate melt in only FeS-added experiments are consistent with the initial compositions with deviations of less than 2 wt % for all analyzed oxides (Table S1).

The SCSS of our experiments varies from 1260 to 5535 ppm (Table 2), and shows a negative relationship with the M/S ratio of the sulfide (Fig. 2A). Twelve experiments that only contained FeS in the initial compositions, exhibit M/S ratios from 0.97 to 1.19, and the experiments with additional Fe metal show higher M/S ratio (1.40 to 1.58; Fig. 2A). The experiments containing both Ni and Fe components in sulfide exhibit even higher M/S (1.34–2.09) and lower measured SCSS (1260–2674 ppm).

4. Discussion

4.1. Approach to equilibrium

We found no compositional variation in quenched silicate melts between different parts of the capsule, as evidenced by the relatively low statistical variations among our EPMA spot analyses (e.g., for S abundance in quenched silicate melts, the 1 sigma uncertainties vary from 1.66 % to 23.14 %, with an average of 6.53 %; Table S1). In addition, the compositions of different sulfide blobs in each experiment were also similar. We further calculated the diffusion coefficients, as well as the diffusion length scale of S, in each experiment, and then compared the diffusion distance to the farthest distances from sulfide melt to the

silicate melt pool (Fig. S2; calculation details are described in Supplementary Materials). Specifically, the distance we measured is the length between the edge of the sulfide blob from which we are primarily obtaining elemental concentrations of the sulfide, typically the largest blob in each experiment, and the boundary of the silicate melt pool that is farthest away from the sulfide. However, there are often multiple sulfide blobs in an experiment (e.g., Fig. 1), and some blobs might be much closer to the boundary of the silicate melt pool. Given that no obvious compositional differences were found among the sulfides in the experiment, the measured distances we plotted in Fig. S2 are the upper limit of diffusion length to reach equilibrium. Nevertheless, the calculated S diffusion length scales for all experiments are distinctly larger than our measured distances, suggesting that the experiments reached equilibrium between the silicate melt and the sulfide melt with respect to S exchange (Fig. S2).

4.2. The oxygen fugacity versus sulfide composition

Brenan et al. (2019) suggested the low fO_2 of the system should enrich the Fe species in the sulfides, decrease the activity of FeS in the sulfides, and, therefore, lower the SCSS. The estimated experimental fO_2s are ~ IW–0.6 to ~ IW–0.2 for experiments coexisting with metallic melts (Method in Supplementary Materials), approaching the fO_2 of the lunar mantle. The experimental fO_2s show a negative correlation with M/S ratios of sulfide (Fig. 2B; Table S1). We further plotted the S solubility experiments with Fe capsule from Brenan et al. (2019) in Fig. 2B, as these experiments were conducted under more reduced conditions (~IW–0.8 to IW–1.5) and also produced sulfides with higher M/S ratio (1.2–6.0). The strong correlation between fO_2 and sulfide M/S suggests the importance of fO_2 controlling the SCSS of silicate melt by changing the FeS activity of the equilibrium sulfide.

We note that the fO_2 is not the only factor controlling the sulfide M/S ratio. With the same initial silicate composition and similar fO_2 conditions, the experiment with the addition of Ni_3S_2 (M/S = 2.0; B663) shows significantly higher M/S ratios than the experiment without
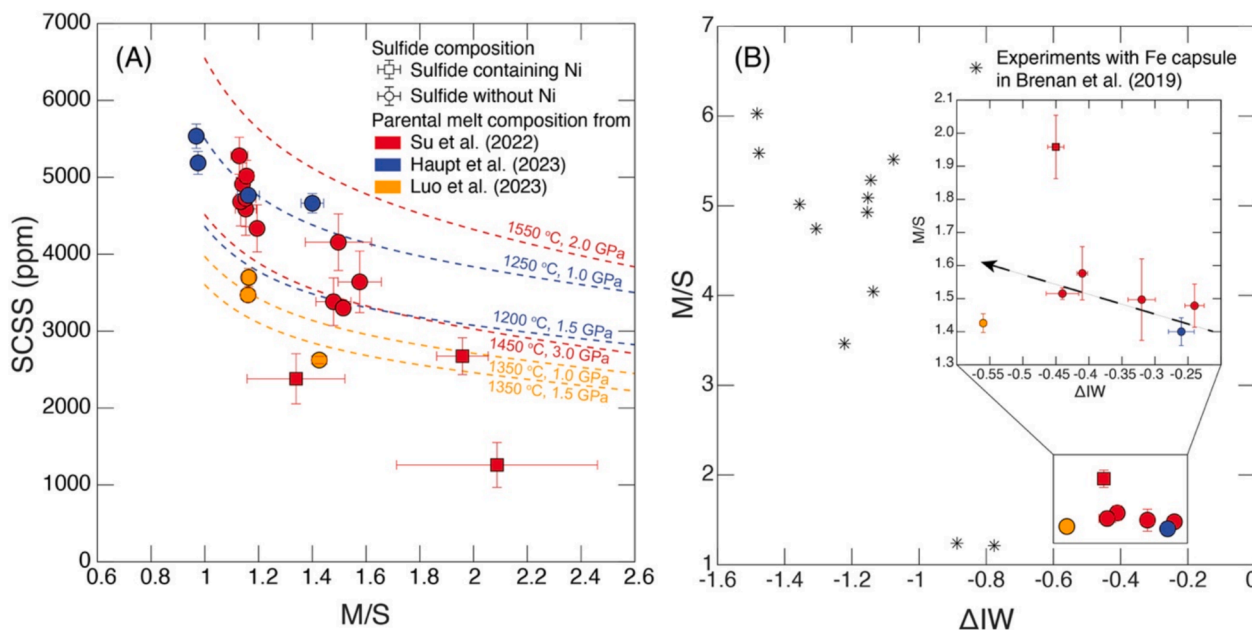

Fig. 2. (A) Metal/silicate (M/S) molar ratio of sulfides versus measured SCSS in this study. The dashed lines indicate the predicted SCSS calculated from the experimental average melt compositions of different CE-5 parental melts and the pressures and temperatures that cover the experimental conditions for each parental melt composition in this study. We varied the M/S ratios of the equilibrium sulfides in our calculations and assumed the sulfides contained only Fe and S to simulate the effect of sulfide compositional variations on SCSS due to changes in fO_2. The results suggest a negative correlation between M/S ratios of sulfides and SCSS in silicate melt. (B) Experimental oxygen fugacity (fO_2) plotted against the M/S ratio of sulfides. The black asterisks represent the S solubility experiments conducted in Fe capsule from Brenan et al. (2019). Two panels suggest good correlations of M/S with fO_2 and SCSS, implying that fO_2 is an important parameter affecting SCSS.

nickel sulfide (M/S = 1.5; B633), emphasizing the role of other metal species in the sulfides, in addition to fO_2, on the M/S ratio. This can be further verified by Ni-bearing experiment B654, which shows the highest M/S ratio (~2.1) and lowest SCSS among our experiments (1260 ppm; Fig. 2A). We were unable to calculate fO_2 for this experiment due to the absence of an immiscible S-poor metal phase. However, the fO_2 of the initial silicate composition of B654 is ~ FMQ-2 and we did not add any Fe metal after precondition. Therefore, the high Ni content in sulfide (50.58 wt%; Table S1), instead of the fO_2, should be responsible for the high M/S ratio, suggesting both lower fO_2 and the involvement of other metal species, such as Ni, in sulfide can increase the M/S of the sulfide, and accordingly significantly lower the SCSS.

4.3. Comparison to previous CE-5 basalt crystallization modeling and experiments

We compared our experimental products that are in equilibrium with pure FeS with equilibrium crystallization modeling and experiments reported by Luo et al. (2023), Haupt et al. (2023), and Su et al. (2022) based on the same compositions of the CE-5 parental melts (Fig. 3). Our experiments are consistent with the pMELTS modeling results in Luo et al. (2023) (yellow dashed lines; Fig. 3), that no mineral crystallized at 1 GPa and 1350 °C, while clinopyroxene is the only mineral phase at 1.5 GPa and 1350 °C. Compared to Haupt et al. (2023), our experiment at 1 GPa and 1250 °C contains a negligible amount of Fe-Ti oxide (Fig. S1A), suggesting that the experiments are close to the liquidus. However, at 1.5 GPa, garnet joined clinopyroxene as a stable phase. The other crystallized phases are in agreement with those in Haupt et al. (2023), but our results imply that the liquidus temperature may be slightly

higher than suggested by Haupt et al. (blue dashed lines; Fig. 3). For experiments with SS0-2, however, our results indicated a multiple saturation point that is ~ 0.5 GPa lower in pressure and ~ 50 °C higher in temperature than those predicted by THERMOCALC modeling of Su et al. (2022) (2.24 GPa and 1472 °C; red dashed lines in Fig. 3), as only the 1.5 GPa/ 1500 °C and 2 GPa/ 1550 °C experiments are superliquidus. In addition, no experiments yielded orthopyroxene as the liquidus phase, and garnet was observed in two experiments at higher pressures. Here, we did not compare the experiments coexisting with high M/S sulfides with previous studies, since in most of these experiments we doped additional Fe metal (Table 1), which would alter the experimental fO_2 and the initial compositions, consequently tending to stabilize mineral phases such as olivine (compare Fig. 1B to 1C; Table 2).

4.4. Previous SCSS models

Previous studies developed terrestrial and lunar-related SCSS models using experimental data as a reliable method to constrain the fate of S during magmatic processes (Blanchard et al., 2021; Ding et al., 2018; Fortin et al., 2015; Liu et al., 2021; O'Neill, 2021; Smythe et al., 2017; Steenstra et al., 2020b). However, most models only considered the effect of Cu and Ni of sulfide on SCSS in addition to pressure, temperature, and silicate melt compositions, ignoring the effect of Fe species in sulfide under low fO_2. The calibration dataset of all these models contains no or very limited experiments under fO_2 below the IW buffer. Therefore, while calculating the activity of FeS in sulfide, these studies only needed to process a FeS-NiS-Cu$_2$S solution without the need to consider metallic Fe species in sulfide liquid. In order to test the fitness of previously developed models to experiments that are in equilibrium with high M/S
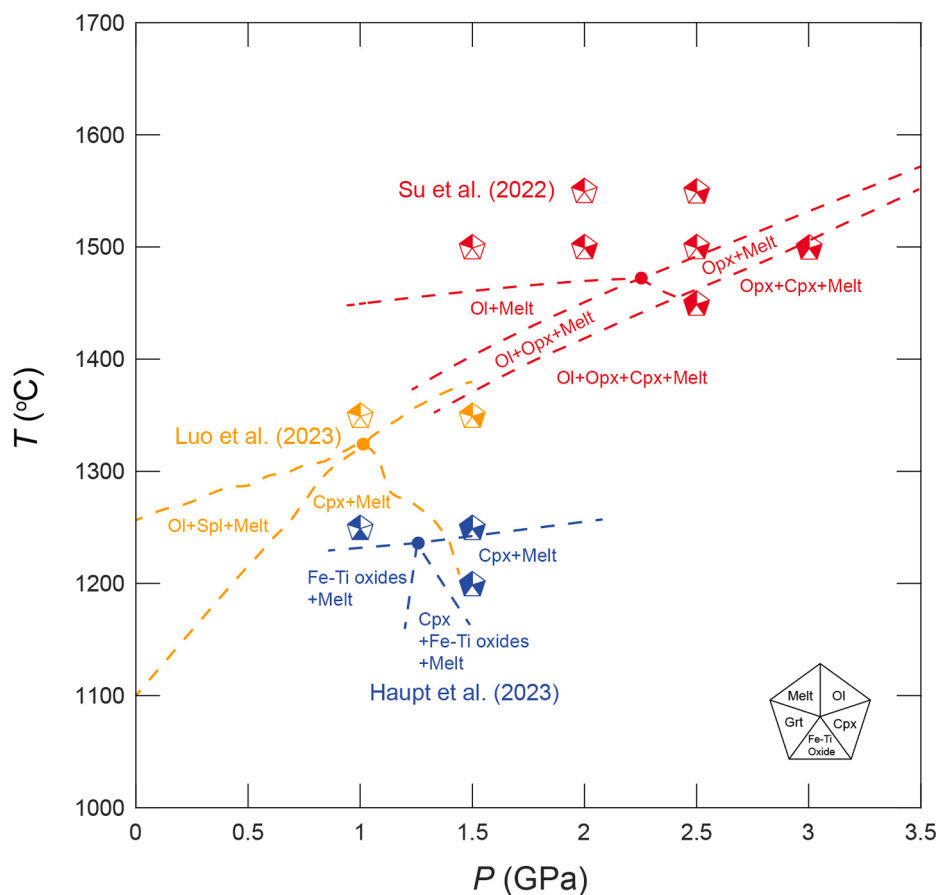

Fig. 3. Pressure–temperature diagram showing experimental phase assemblages in equilibrium with pure FeS liquid. Symbols in different colors represent experimental results in this study using different starting mix compositions, constructed based on the parental magma compositions from Luo et al. (2023), Haupt et al. (2023), and Su et al. (2022). Dashed lines are phase relations reported by those studies, plotted for comparison.

ratio sulfides under low experimental fO_2, we applied seven models to the experiments reported by Brenan et al. (2019) and this study. The results show that previous models generally have good fitness to experiments with sulfide M/S ratios close to 1. However, obvious overestimations are observed in all models when predicting experiments with higher M/S ratio sulfides (Fig. 4). Brenan et al. (2019) applied an asymmetric solution model and calculated the activities of Fe and FeS in sulfides by parameters from Buono and Walker (2011) for lunar environment. However, the sulfides in the lunar returned samples indeed contain a certain amount of other metal elements [e.g., chalcopyrite ($CuFeS_2$), cubanite ($CuFe_2S_3$), and pentlandite ($(Fe,Ni)_9S_8$); Liu et al., 2022; Taylor and Williams, 1973], which makes the model applied in Brenan et al. (2019) not optimally suitable for complex composition of lunar sulfides. Please note that experiments conducted under fO_2s much lower than the lunar environment (e.g., Mercury conditions) and related SCSS models were not considered here (e.g., Chabot et al., 2014; Namur et al., 2016b; Vander Kaaden and McCubbin, 2016), as these models will greatly underestimate our experiments and those in Brenan et al. (2019) (e.g., Fig. S3). The reason is these models were calibrated under very reducing conditions (~IW–5) that the presence of (Mg,Ca,Fe)S in both sulfide and silicate melt is expected (Malavergne et al., 2014; Namur et al., 2016a), but there is no evidence of this in the lunar mantle.

4.5. Thermodynamic background on SCSS

Motivated by the above, here we developed a new thermodynamic SCSS model that is applicable to lunar-relevant sulfide compositions and fO_2s. The equilibrium relationship between S in the silicate melt and immiscible sulfide can be described as:

$$FeO_{silicate\ melt} + \frac{1}{2}S_2 = FeS_{sulfide} + \frac{1}{2}O_2 \tag{1}$$
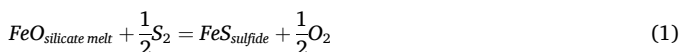
while at the equilibrium, the SCSS can be expressed as the equation (e.g., Smythe et al., 2017; Ding et al., 2018):

$$\ln[S]_{SCSS} = \frac{\Delta G^o}{RT} + lnC_s - lna_{FeO}^{silicate} + lna_{FeS}^{sulfide} \tag{2}$$

where $[S]_{scss}$ is sulfur concentration in the silicate melt at sulfide saturation, ΔG^o is the Gibbs free energy of Eq. (1), R is the gas constant, T is the temperature, and C_s is the sulfur capacity, which is defined as (e.g., Smythe et al., 2017):

$$lnC_s = \ln[S] + 0.5ln\left(\frac{fO_2}{fS_2}\right) \tag{3}$$

where fO_2 and fS_2 are fugacities of O_2 and S_2. The C_s can be expressed with the form (O'Neill and Mavrogenes, 2002):

$$lnC_s = A_o + \sum_{M}X_MA_M\Big/T \tag{4}$$

where A_o is a constant, while X_M and A_M are mole fraction of cation M in the silicate melt and corresponding coefficient. For ΔG^o, it should be a function of equilibrium temperature (T) and pressure (P):

$$\frac{\Delta G^o}{RT} = \frac{\Delta H^o}{RT} - \frac{\Delta S^o}{R} + \frac{P\Delta V^o}{RT} \tag{5}$$

where ΔH^o, ΔS^o, and ΔV^o are enthalpy, entropy and molar volume terms of Eq. (1). In Eq. (2), the remaining terms that need to be constrained are $a_{FeO}^{silicate}$ and $a_{FeS}^{sulfide}$. The $a_{FeO}^{silicate}$ can be described as a function of mole fractions of Fe and Ti in the silicate melt (O'Neill and Mavrogenes, 2002):

$$a_{FeO}^{silicate} \sim X_{Fe}X_{Ti} \tag{6}$$

while by assuming a four-component (Fe-FeS-Cu_2S-NiS) symmetric
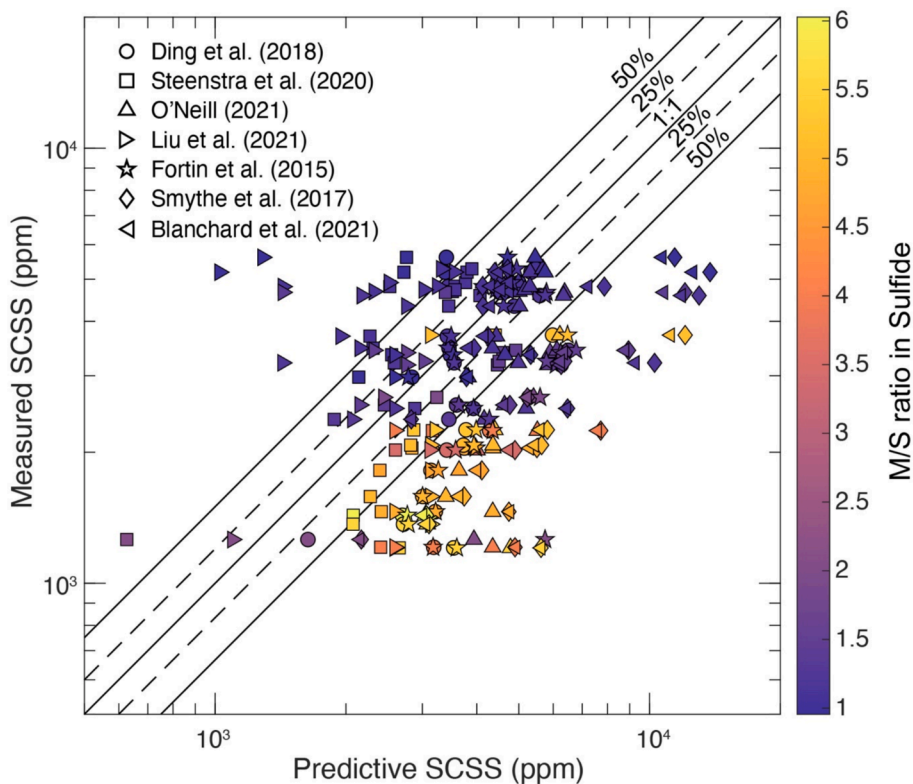
Fig. 4. The comparison between SCSS predicted by previously developed models and the measured SCSS in the lunar-relevant experiments from Brenan et al. (2019) and this study. Previously developed models typically show good agreement with experimentally-determined SCSS where the sulfides' M/S ratio are close to unity (violet symbols), but exhibit overall overestimations of SCSS for equilibrium with sulfides with M/S > 1 (red to yellow symbols).

solution, the $a_{FeS}^{sulfide}$ can be expressed as (Wood and Fraser, 1977):

$$ln a_{FeS}^{sulfide} = ln X_{FeS}^{sulfide} + \frac{W_{FeS-NiS}}{RT}(X_{NiS}^{sulfide\,2}) + \frac{W_{FeS-Fe\,metal}}{RT}(X_{Fe\,metal}^{sulfide\,2})$$
$$+ \frac{W_{FeS-CuS_{0.5}}}{RT}(X_{CuS_{0.5}}^{sulfide\,2})$$
$$+ \frac{(W_{FeS-NiS} + W_{FeS-Fe\,metal} - W_{NiS-Fe\,metal})}{RT}(X_{NiS}^{sulfide} X_{Fe\,metal}^{sulfide})$$
$$+ \frac{(W_{FeS-NiS} + W_{FeS-CuS_{0.5}} - W_{NiS-CuS_{0.5}})}{RT}(X_{NiS}^{sulfide} X_{CuS_{0.5}}^{sulfide})$$
$$+ \frac{(W_{Fe-Fe\,metal} + W_{FeS-CuS_{0.5}} - W_{Fe\,metal-CuS_{0.5}})}{RT}(X_{Fe\,metal}^{sulfide} X_{CuS_{0.5}}^{sulfide})$$

$$(7)$$

where W_{i-j} is the interchange energy for i-j exchanges. Because the number of experiments containing excess Ni in sulfide in previous studies is very limited, we did not separate Ni as a species other than NiS in our model. Combing Eqs. (4)–(7) into (2), we can predict SCSS as:

$$ln[S]_{SCSS}(ppm) = A + \frac{B}{T} + \sum C_i X_i + D X_{Fe} X_{Ti} + E\frac{P}{T} + ln X_{FeS}^{sulfide} + \frac{F}{T}(X_{NiS}^{sulfide\,2})$$
$$+ \frac{G}{T}(X_{Fe\,metal}^{sulfide\,2}) + \frac{H}{T}(X_{CuS_{0.5}}^{sulfide\,2}) + \frac{I}{T}(X_{NiS}^{sulfide} X_{Fe\,metal}^{sulfide})$$
$$+ \frac{J}{T}(X_{NiS}^{sulfide} X_{CuS_{0.5}}^{sulfide}) + \frac{K}{T}(X_{Fe\,metal}^{sulfide} X_{CuS_{0.5}}^{sulfide})$$

$$(8)$$

where $A - K$ are coefficients.

In Eq. (8), we need to calculate the mole fractions of four components (Fe, FeS, Cu$_2$S, and NiS) in the sulfides. The preference of different polyvalent cations to bond with S in the sulfides under different fO_2 is unknown. Therefore, as the first order constraint, here we assume that all cations (e.g., Fe, Cu, Ni) tend to bond with anions (e.g., S and O) in proportion to their analyzed molar amounts:

$$X_{FeS}^{sulfide} = n_S^{sulfide} \frac{n_{Fe}^{sulfide}}{n_{Fe}^{sulfide} + n_{Ni}^{sulfide} + n_{Cu}^{sulfide}}$$

$$(9)$$

$$X_{CuS_{0.5}}^{sulfide} = n_S^{sulfide} \frac{n_{Cu}^{sulfide}}{n_{Fe}^{sulfide} + n_{Ni}^{sulfide} + n_{Cu}^{sulfide}}$$

$$(10)$$

$$X_{NiS}^{sulfide} = n_S^{sulfide} \frac{n_{Ni}^{sulfide}}{n_{Fe}^{sulfide} + n_{Ni}^{sulfide} + n_{Cu}^{sulfide}}$$

$$(11)$$

where $n_{Fe}^{sulfide}$, $n_{Ni}^{sulfide}$, $n_{Cu}^{sulfide}$, $n_S^{sulfide}$ represent the mole numbers of Fe, Ni, Cu, and S in the sulfide. Thereby, the mole fraction of Fe metal in sulfide $X_{Fe\,metal}^{sulfide}$ can be calculated by:

$$X_{Fe\,metal}^{sulfide} = \frac{n_{Fe}^{sulfide} - \left(n_S^{sulfide} + n_O^{sulfide}\right)\frac{n_{Fe}^{sulfide}}{n_{Fe}^{sulfide} + n_{Ni}^{sulfide} + n_{Cu}^{sulfide}}}{n_{Fe}^{sulfide} + n_{Ni}^{sulfide} + n_{Cu}^{sulfide}}$$

$$(12)$$

where $n_O^{sulfide}$ represents the mole fraction of O element in the sulfide.

4.6. Calibrating dataset for predictive SCSS model

In order to develop the predictive SCSS model, we compiled data from 361 experiments as the calibration dataset (Brenan, 2008; Brenan et al., 2019; Ding et al., 2014; Ding et al., 2018; Gaetani and Grove, 1997; Grewal et al., 2019; Holzheid and Grove, 2002; Kiseeva and Wood, 2013; Kiseeva and Wood, 2015; Li and Agee, 1996; Li and Audétat, 2012; Liu et al., 2007; Peach and Mathez, 1993; Ripley et al., 2002; Smythe et al., 2017; Steenstra et al., 2018; Steenstra et al., 2020a; Steenstra et al., 2020b; Tsuno et al., 2018; Wohlers and Wood, 2015; this study). The calibration dataset is listed in Table S2 and the P-T-fO_2-composition ranges of these data are described in Fig. 5.

Seven studies had experiments that did not report sulfide compositions and therefore these experiments were not included in our model calibration dataset (Fortin et al., 2015; Mavrogenes and O'Neill, 1999; O'Neill and Mavrogenes, 2002; Jugo et al., 2005; Liu et al., 2007; Righter et al., 2009; Wykes et al., 2015). However, we treat them as an extrapolation dataset to test the fitness of our model (Table S3). These experiments only added pure FeS in the starting materials, hence the sulfide composition can be estimated following the method adopted by Steenstra et al. (2018), that the abundance of Fe in sulfide is assumed to be 63.5 wt%, the O in sulfide is calculated by the empirical equation $O_{sulfide}(wt.\%) = 0.24 \times FeO_{silicate}(wt.\%)$ (Kiseeva and Wood, 2015), and the S in sulfide is $S_{sulfide}(wt.\%) = 1 - O_{sulfide}(wt.\%) - Fe_{sulfide}(wt.\%)$. We did not compile experiments from Blanchard et al. (2021) because the pressures and temperatures of their experiments (7 – 23 GPa; 1900 –
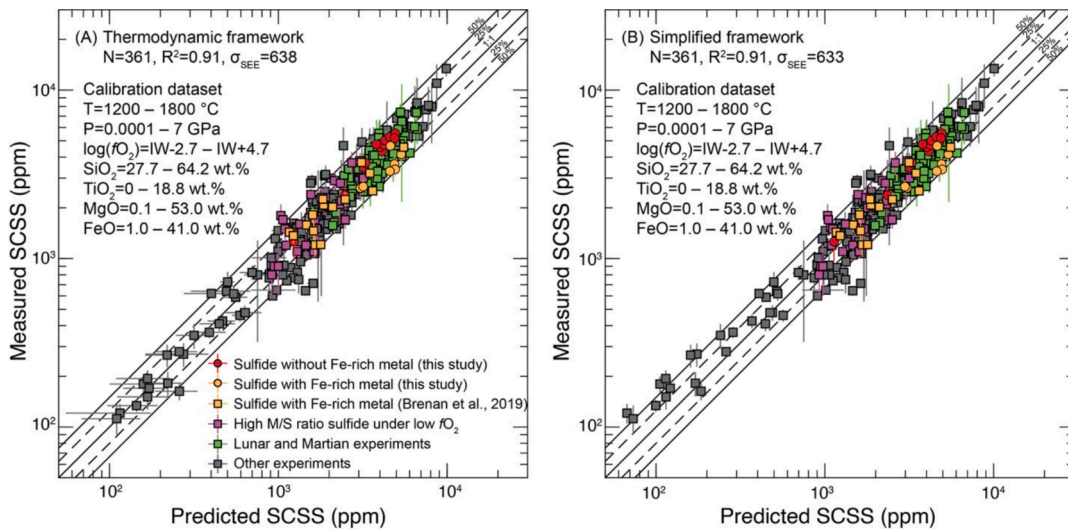

Fig. 5. Comparison between measured and predicted SCSS of 361 experiments from this study and previous studies. The predictions are calculated by (A) Eq. (13), and (B) Eq. (14). The error bar represents one sigma error. The purple squares represent SCSS data from alloy-silicate S partitioning under low fO_2 (logfO_2 < IW) where silicate melts coexisted with high M/S ratio sulfides (Grewal et al., 2019; Tsuno et al., 2018). σ_{SEE} denotes the standard error of the estimate, which is calculated by first computing the sum of squared residuals between measured and predicted SCSS values, dividing this sum by the degrees of freedom, and then taking the square root of the result. All data are given in Table S2.

2350 °C) are designed for the scenario such as the deep magma ocean of proto-Earth instead of mantle melting conditions of terrestrial bodies, and therefore conducted at much higher pressures and temperatures than those of our calibrated dataset (0.0001 – 7 GPa; 1200 – 1800 °C). Wendlandt (1982) did not report the silicate melt and sulfide composition of their experimental products. For some unknown reason, experiments in Wood and Kiseeva (2015) show anomalously high S concentrations in their experiments, even for experiments without Fe-Si alloy (e.g., Experiment 1325 with S of 18700 ppm), which is abnormal compared to the experiments with similar *P-T*-composition conditions [e.g., Experiment D0063 from Wykes et al. (2015) with S of 5663 ppm]. Therefore, we did not include their data.

4.7. A new SCSS model

By applying the above thermodynamic framework (Eq. (8)) to our calibration dataset (Table S2), we obtain the following model with the best fitting quality:

$$
\begin{aligned}
\ln[S]_{SCSS}(ppm) =\ & 13.81(\pm 0.58) - \frac{5311(\pm 307)}{T} + 0.17(\pm 1.29)X_{Ti} \\
& + 0.21(\pm 0.53)X_{Ca} - 4.42(\pm 0.62)X_{Si} - 4.35(\pm 0.66)X_{Al} \\
& + 4.30(\pm 0.58)X_{Fe} - 2.40(\pm 0.53)X_{Mg} \\
& - 9.70(\pm 6.76)X_{Fe}X_{Ti} - 315(\pm 23)\frac{P}{T} + \ln X_{FeS}^{sulfide} \\
& + \frac{-353(\pm 1526)}{T}\left(X_{NiS}^{sulfide\,2}\right) + \frac{2026(\pm 187)}{T}\left(X_{Fe\,metal}^{sulfide\,2}\right) \\
& + \frac{3433(\pm 3718)}{T}\left(X_{CuS_{0.5}}^{sulfide\,2}\right) \\
& + \frac{3541(\pm 3706)}{T}\left(X_{NiS}^{sulfide}X_{Fe\,metal}^{sulfide}\right) \\
& + \frac{14561(\pm 9401)}{T}\left(X_{NiS}^{sulfide}X_{CuS_{0.5}}^{sulfide}\right) \\
& + \frac{-9987(\pm 14814)}{T}\left(X_{Fe\,metal}^{sulfide}X_{CuS_{0.5}}^{sulfide}\right)
\end{aligned}
\tag{13}
$$

where *T* is in Kelvin, and *P* is in GPa. Values in parentheses are 1σ uncertainties in the model coefficients. By applying the model, the predicted SCSS can fit the measured values well ($R^2 = 0.91$; $\sigma_{SEE} = 638$), and almost all experiments can be reproduced within 50 % uncertainties (Fig. 5A). As we discussed above, the high M/S ratio of sulfide is not necessarily a signature of low *f*O$_2$, as the existence of other metal cations in sulfides (e.g., Ni, Cu) can also increase the M/S ratios (e.g., Ripley et al., 2002; Steenstra et al., 2020b). Therefore, we separately marked all experiments that coexisted with Fe metal (Brenan et al., 2019; this study) and experiments from S partitioning experiments with high M/S sulfides under reduced conditions (IW–2 < log*f*O$_2$ < IW) (Grewal et al., 2019; Tsuno et al., 2018). The model exhibits a good fit to these experiments under low *f*O$_2$ (Fig. 5A), which makes our model more accurate in predicting SCSS under lunar mantle-relevant *f*O$_2$ than all previous models.

To test our model, we calculated the predictive SCSS based on experiments in this study as a function of the M/S ratio of sulfides (Fig. 2A). For each parental magma composition, we utilized the average melt composition (Table S1), and plotted the SCSS trend in two *P-T* conditions covering the experimental temperatures and pressures, assuming that the sulfides contain only Fe and S, to investigate the effect of sulfide M/S ratio caused by changes in *f*O$_2$ without varying the FeO* content in silicate melt. Our calculations can constrain the experimental results well, which show that the M/S ratio of the sulfides negatively correlates with the SCSS. We further compared our new model with seven previously developed SCSS models (Blanchard et al., 2021; Ding et al., 2018; Fortin et al., 2015; Liu et al., 2021; O'Neill, 2021; Smythe et al., 2017; Steenstra et al., 2020b). The new SCSS model developed in this study yielded a higher coefficient of determination (R^2) than all

other models for our calibration dataset, indicating our model predicts SCSS well under a wide range of conditions (see Fig. 5 or S4 for the *P-T*-*f*O$_2$-composition ranges of our calibration data).

We conducted *t*-test for parameters in Eq. (13) and p values of 8 parameters (X_{Ti}, X_{Ca}, $X_{Fe}X_{Ti}$, $X_{NiS}^{sulfide\,2}$, $X_{CuS_{0.5}}^{sulfide\,2}$, $X_{NiS}^{sulfide}X_{Fe\,metal}^{sulfide}$, $X_{Fe\,metal}^{sulfide}X_{CuS_{0.5}}^{sulfide}$) are larger than 0.05 threshold (5 % significance level), suggesting the overfitting of the model based on the thermodynamic framework. Meanwhile, we also noticed that 6 terms in Eq. (13) have significant 1σ uncertainties (X_{Ti}, X_{Ca}, $X_{NiS}^{sulfide\,2}$, $X_{CuS_{0.5}}^{sulfide\,2}$, $X_{NiS}^{sulfide}X_{CuS_{0.5}}^{sulfide}$, $X_{NiS}^{sulfide}X_{Fe\,metal}^{sulfide}$, $X_{Fe\,metal}^{sulfide}X_{CuS_{0.5}}^{sulfide}$), suggesting the relative unimportance of these terms for the fitness. Therefore, we omitted these 6 terms and refined the model with a simplified expression:

$$
\begin{aligned}
\ln[S]_{SCSS}(ppm) =\ & 14.03(\pm 0.31) - \frac{5417(\pm 284)}{T} - 4.60(\pm 0.37)X_{Si} \\
& - 4.49(\pm 0.44)X_{Al} + 4.24(\pm 0.30)X_{Fe} \\
& - 2.53(\pm 0.29)X_{Mg} - 9.20(\pm 2.30)X_{Fe}X_{Ti} \\
& - 320(\pm 22)\frac{P}{T} + \ln X_{FeS}^{sulfide} + \frac{2051(\pm 178)}{T}\left(X_{Fe\,metal}^{sulfide\,2}\right) \\
& + \frac{16080(\pm 7746)}{T}\left(X_{NiS}^{sulfide}X_{CuS_{0.5}}^{sulfide}\right)
\end{aligned}
\tag{14}
$$

For the simplified version of our SCSS model, the comprehensive fitness to all 361 experiments is still good ($R^2 = 0.91$; $\sigma_{SEE} = 633$), including those experiments coexisting with Fe-rich metal (orange symbols; Fig. 5B). Overall, the two forms show especially good agreement when predicting SCSS under *f*O$_2$ below IW buffer, as most of the SCSS values of these experiments can be reproduced within 25 % deviation by both forms (orange symbols in Fig. 5), which makes our model very suitable for lunar mantle conditions. In addition, we conducted the *t*-test again and the p values of all parameters are less than 0.05, suggesting all parameters in Eq. (14) are statistically significant. However, we indeed observed that Eq. (14) did not perform as well as Eq. (13) for some of the low-SCSS experiments. Therefore, we reported both versions and made them available as SCSS calculators in a MS Excel spreadsheet in Table S3.

To further assess the quality of our new SCSS model, we tested the model with 120 additional SCSS experiments in our extrapolation dataset. The fitness of our predictions to the SCSS measured in these experiments by Eqs. (13) ($R^2 = 0.85$; $\sigma_{SEE} = 507$) and (14) ($R^2 = 0.85$; $\sigma_{SEE} = 496$) remains good, indicating the reliability of our model (Fig. S5; Table 3). We noticed that the effect of *f*O$_2$ on SCSS observed in Mercury-related experiments is opposite to Fig. 2, i.e., SCSS significantly increases as *f*O$_2$ decreases (e.g., Chabot et al., 2014). That is because at such reduced systems (~IW–5), S would not complex primarily with Fe^{2+} in the silicate melt, since the large amount of the Fe^{2+} would be reduced to Fe metal, that S would prefer to form MgS and CaS complexes (Namur et al., 2016a). In this case, applying Eq. (2) is not appropriate and the estimations of activity coefficients of MgO and CaO in silicate melt, as well as MgS and CaS in sulfide melt are required. These will significantly complicate our SCSS model and inevitably propagate uncertainties. Given the composition of lunar sulfides are composed primarily of Fe, Ni and Cu, instead of Mg and Ca (Malavergne et al., 2014), and the lunar mantle *f*O$_2$ is much higher than that of Mercury (Wadhwa, 2008), we did not include experiments with extremely low *f*O$_2$ into our calibration dataset. However, we tested four experiments from Mercury-relevant studies (Chabot et al., 2014; Berthet et al., 2009), all of which were subsets that were free of metallic Si in the starting composition (*f*O$_2$s from IW–1.6 to IW–0.7; Berthet et al., 2009), thus avoiding the involvement of significant amounts of Mg and Ca in the sulfide. All four experiments can be reproduced within 50 % uncertainties (Fig. S5).

4.8. Sulfur abundance in the mantle source of CE-5 basalt

The new SCSS model developed in this study allows us to track the S concentrations in the lunar mantle-derived melts with various source sulfide compositions, abundance, and the extent of mantle melting. To begin with, we can calculate the SCSS of the parental melt of CE-5 basalts, and compare our calculations to the reconstructed S concentrations in the parental magma based on the proposed petrogenesis (e.g., Tian et al., 2021; Wang et al., 2024a), in order to assess whether the melting residue is sulfide-bearing. Generally, the multiple saturation point may indicate the pressure and temperature at which the parental melt was finally in equilibrium with the mantle source (e.g., Grove and Krawczynski, 2009). Therefore, we applied the multiple saturation point conditions and parental magma compositions from Haupt et al. (2023), Luo et al. (2023), and Wang et al. (2024a) in our calculations first, as all of them suggested the CE-5 mantle source is relatively shallow (~100–250 km), and the most primitive CE-5 basaltic clasts may be products of mantle partial melting.

The S concentrations in CE-5 mare basalt have been estimated by several previous studies [e.g., 600 ± 300 ppm in Liu et al. (2022); ~760–1720 ppm in Li et al. (2024); ~1107–1351 ppm in Che et al. (2021)]. Sulfur abundances reported by Che et al. (2021) and Li et al. (2024) are about twice as high as those calculated by Liu et al. (2022). However, the higher S abundances may reflect the fractional crystallization process of the CE-5 parental melt, which is suggested by the relatively low MgO concentrations of clasts in Che et al. (2021) (4.49–5.17 wt%) and Li et al.(2024) (4.58–7.28 wt%; measurements from Wang et al., 2023), as the MgO content of CE-5 basalt can be as high as 9.71 wt% (Tian et al., 2021). In addition, neither Che et al. (2021) nor Li et al. (2024) evaluated the loss of S by possible equilibrium degassing (Liu et al., 2022; Wang et al., 2024b). Based on the above

arguments, we applied the lower estimation by Liu et al. (2022) in our following calculations.

We tested three possible sulfide compositions. In addition to pure FeS (e.g., Ding et al., 2018), and high Fe/S ratio sulfide to simulate low fO_2 environment (M/S = 6 at fO_2 = IW–1.48; Brenan et al., 2019), we examined a high M/S ratio sulfide with 12 wt% Ni (the possible upper bound of Ni content in lunar mantle sulfide calculated by mass balance; Brenan et al., 2019), as the existence of Ni and Cu in sulfide will further lower the SCSS (e.g., Smythe et al., 2017). The calculations show that the predictive SCSS for all simulated scenarios is higher than the concentration of S in the CE-5 parental melt (Fig. 6), indicating the mantle residue was likely sulfide-absent at the point of CE-5 basalt extraction unless the Ni distribution in the lunar mantle is heterogeneous so that an extremely S-poor and Ni-rich, Fe-alloy was the chief S-bearing accessory phase in the CE-5 mantle source (e.g., M/S = 6 sulfide with ~ 20 wt% Ni). Liu et al. (2022) and Wang et al. (2024b) reported the sulfide composition in CE-5 basaltic clasts and impactites. After the exclusion of exotic S-bearing phases, Ni-enriched sulfide (e.g., Pentlandite) was only observed in the interior of the troilite and interpreted as an exsolution phase. Considering the relatively low Ni abundance of the CE-5 primitive magma (50 – 100 ppm) compared with the Apollo low-Ti basalt (Su et al., 2023), it is unlikely that the Ni-enriched and S-depleted alloy was the dominant S-bearing accessory phase in the CE-5 mantle source.

We take the petrogenesis from Wang et al. (2024a) as an example to reconstruct the S abundance in a shallow mantle source scenario. These authors suggested the CE-5 mare basalt was generated by ~ 2–5 % partial melting of a pyroxenitic mantle. We simplified the melting process as modal batch melting and applied the equation:

$$C_o^S = C_L^S \times \left(D_{Bulk}^S + F(1 - D_{Bulk}^S) \right) \tag{15}$$

where F represents the melting degree, D_{Bulk}^S represents the partition
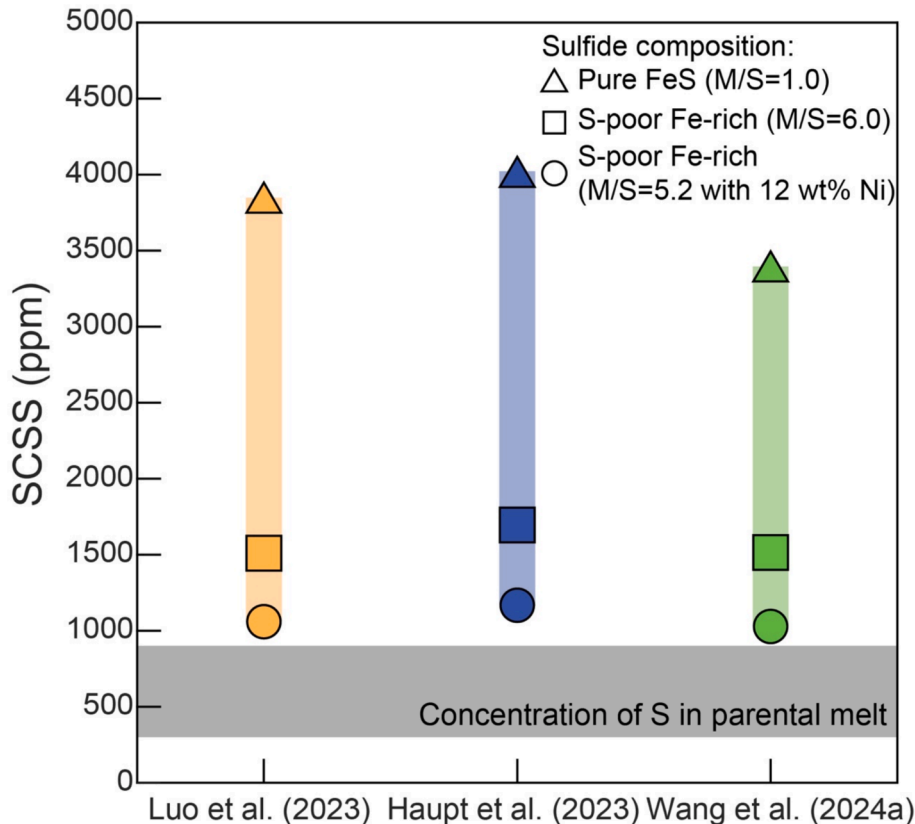

Fig. 6. Predictive SCSS for different CE-5 parental magma compositions and three possible equilibrium sulfide compositions. Also plotted is the calculated range of S concentrations in the CE-5 mare basalt prior to equilibrium degassing (Liu et al., 2022), to represent the S in the parental melt, since the premise for all parental melt compositions here is that the most primitive CE-5 mare basalt is the direct product of mantle partial melting (Haupt et al., 2023; Luo et al., 2023; Wang et al., 2024a).

coefficient S during partial melting, that we take D = 0.001 as suggested by Steenstra et al. (2020b) in lunar magma ocean modeling, C_o^S and C_L^S are concentrations of S in the mantle source and partial melts, respectively. We note that the Eq. (15) applies where the extent of melting is larger than needed to consume sulfide from the lunar mantle residue. The results suggest the S concentration in the CE-5 mantle source is ~ 13–31 ppm (Fig. 7A) if the mantle source underwent 2–5 % partial melting to produce CE-5 mare basalt (Wang et al., 2024a).

Tian et al. (2021) suggested the CE-5 basalt is a product of source partial melting followed by extensive fractional crystallization of the primary basalt. This hypothesis has been further verified by Su et al. (2022) and Haupt et al. (2023), proposing a deep mantle source origin (e.g., ~500 km depth; Su et al., 2022). A recent study by Li et al. (2024) reported the estimated S abundance in the CE-5 mantle source can be as high as ~ 125 ppm if the CE-5 basalt originated from a deep source (Su et al., 2022), which overlaps with the S budget in Earth's upper mantle (Ding and Dasgupta, 2017). Such a high lunar mantle S abundance was calculated from the SCSS of the immiscible mafic melt observed in their basaltic clasts (containing 2500 ppm S), which must be accompanied by extensive fractional crystallization and therefore cannot represent the primitive mantle-derived melt. Moreover, in their calculation they also assumed the mantle source experienced 10 % of partial melting followed by 30–70 % of fractional crystallization (Su et al., 2022). However, the calculated S abundance by magmatic differentiation reconstruction is highly model-dependent (Li et al., 2024). The major element modeling in Su et al. (2022) could provide valuable insights regarding mantle source compositions and melting conditions, but it cannot constrain the mantle melting process well, as their THERMOCALC model suggests the feasible melting degrees are in the range of 1–25 %. That is, the S content of the parental magma can vary up to a factor of ~ 25 over such a large range of partial melting estimation if sulfide in mantle residue was exhausted (Eq. (15)). Because of above, we tested the deep source hypothesis with the parental magma composition from Su et al. (2022) but assumed the mantle source experienced 2–3 % of partial melting, followed by 43–88 % of fractional crystallization based on the trace element modeling by Tian et al. (2021). The S abundance in the parental magma before fractional crystallization can be estimated by Rayleigh fractionation:

$$C_L^S = \frac{C_l^S}{F^{\left(D_{Bulk}^S - 1\right)}} \tag{16}$$

where F represents the fraction of melt during magma differentiation, while C_L^S and C_l^S are concentrations of S in the parental and evolved melts. The calculated S in the parental magma is 72–342 ppm, which is distinctly lower than the SCSS calculated using our predictive model based on the composition of the parental melt (~1130–4280 ppm). Considering our experiments with parental magma similar to Su et al. (2022) suggested a multiple saturation point with an even higher temperature and lower pressure (Fig. 3), which will further increase the SCSS of the parental melt (Eqs. 13 and 14), if the mantle source residue of CE-5 basalt is deep, then it must be sulfide-absent. In this case, the calculated S abundance in the mantle source is ~ 2–11 ppm (Fig. 7B).

4.9. Comparison of the sulfur abundance in the mantle source of CE-5 versus Apollo basalts

Comparison of our calculated source S abundances with those in the source of older Apollo samples can provide insights into lunar mantle S evolution. Previous studies applied magmatic differentiation reconstruction (e.g., Hauri et al., 2011) or conservative elemental ratios (e.g., Ni et al., 2019; Su and Zhang, 2024) to calculate the volatile abundance in the mantle source of older Apollo samples, with the former method demanding the knowledge of magma evolution path, and the latter approach requiring the determination of specific refractory element abundances in the mantle source. Ding et al. (2018) estimated S concentrations in the mantle sources of various Apollo basalts and volcanic glasses by estimating the melting degrees of their sources. The results show the S abundances in the mantle source are 25–120 ppm for Apollo low-Ti basalts and green glasses, and 10–157 ppm for high-Ti basalts and orange glasses (Fig. 8). These authors proposed a heterogeneous S distribution in the lunar mantle, since even samples with similar Ti contents have distinct S abundances (e.g., the source of Apollo 12 and 15 low-Ti basalts have 27–92 and 10–23 ppm S, respectively). However, the uncertainties of melting degree estimation and S degassing calibration may also contribute to this heterogeneity. Ni et al. (2019) found similarities in the highest S/Dy ratios of melt inclusions in different low-
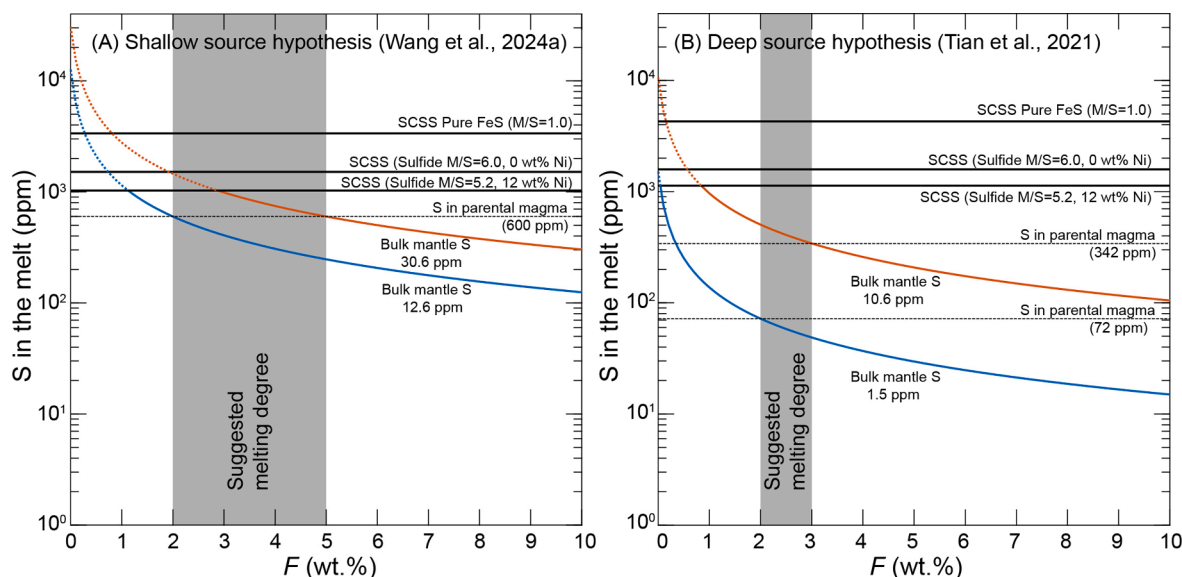
Fig. 7. The evolution of S content in the melt as a function of partial melting degree (F in wt.%) of the CE-5 (A) shallow mantle source or (B) deep mantle source. The blue and orange solid lines represent the S concentration in the partial melts after consumption of sulfide, while blue and orange dashed lines indicate S contents of partial melts if the mantle residue was not saturated with a high M/S (5.2) sulfide with 12 wt% Ni. Black solid lines are predictive SCSS for different sulfide compositions. Black dotted lines and grey vertical bands represent the S concentration in the CE-5 parental melt and the estimated degrees of partial melting as suggested by Wang et al. (2024a) and Tian et al. (2021).
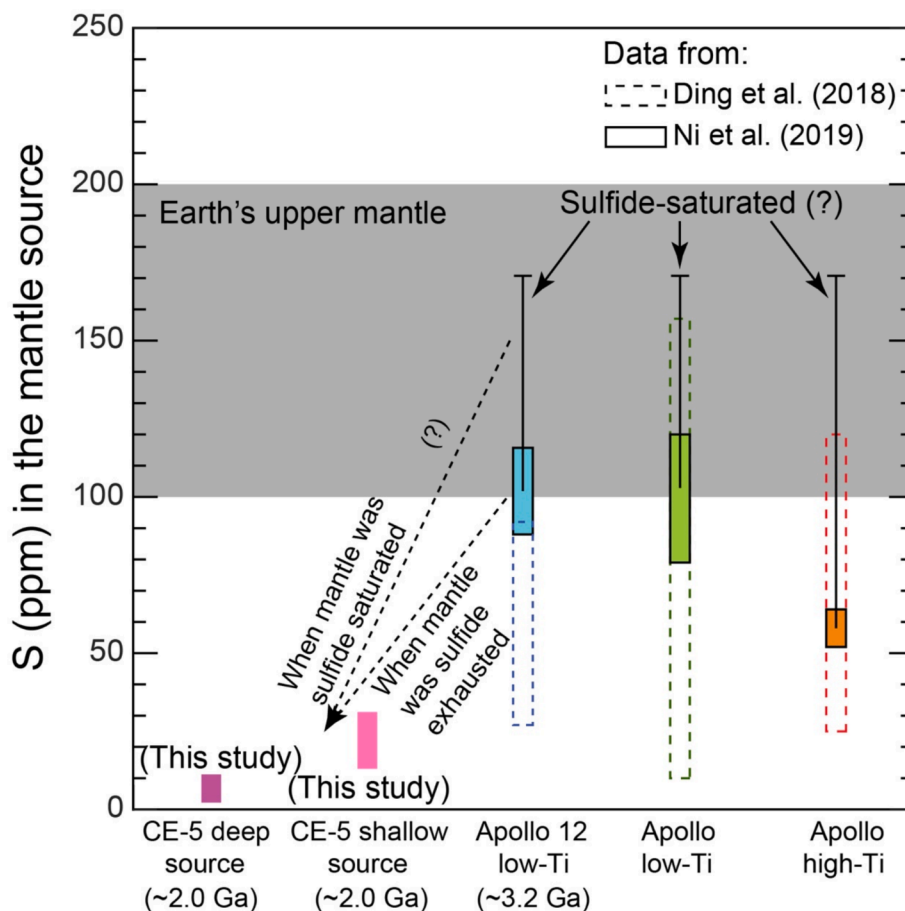
Fig. 8. The calculated S abundance in the mantle of CE-5 mare basalt compared to those estimated by Ding et al. (2018) and Ni et al. (2019) for the Apollo high-Ti and low-Ti mare basalts source. In particular, we plotted the predicted S abundances in the source of Apollo 12 low-Ti basalts. The estimates of S abundances in mantle source of Apollo samples are based on the premise that the mantle residue was sulfide-absent. The error bars are schematic, indicating the S abundance in the mantle would be higher than those estimations if the mantle residue is sulfide-saturated (e.g., Brenan et al., 2019). The deep source petrogenesis applied in the calculations are from Tian et al. (2021), while the shallow source hypothesis is from Wang et al. (2024a). The S abundance in the Earth's upper mantle is from Ding and Dasgupta (2017). The age of Apollo 12 low-Ti basalt (Alexander Jr et al., 1972; Compston et al., 1971; Stettler et al., 1973) is the average of samples investigated in Ding et al. (2018) and Ni et al. (2019).

Ti basalts, a phenomenon also found among high-Ti samples, and that the highest S/Dy ratios of inclusions in the low-Ti basalts appeared to be systematically higher than in the high-Ti samples (e.g., Hauri et al., 2015). They regarded the highest S/Dy as the best estimate of this ratio for the parental magma before degassing, and applied a bulk silicate Earth Dy concentration (McDonough and Sun, 1995) to calculate S abundances of 79–120 and 52–64 ppm in the mantle source of low-Ti and high-Ti samples, respectively (Fig. 8).

The source of the young CE-5 basalt shows overall much lower S abundances compared to the mantle of the Apollo low- and high-Ti samples. This is interesting as Tian et al. (2021), Haupt et al. (2023), and Luo et al. (2023) suggested the mantle of CE-5 basalts might be similar to that of Apollo 12 low-Ti basalts in terms of isotopic and major element geochemistry. We plotted the S abundances in the mantle of Apollo 12 low-Ti basalts from Ding et al. (2018) (27–92 ppm) and Ni et al. (2019) (88–116 ppm), and found that the S abundances in the CE-5 mantle is a factor of ~ 3–80 lower compared to those reported by Ni et al. (2019), depending on the petrogenesis of CE-5 basalts. Only when the mantle source is shallow, can the upper limit of the CE-5 mantle S abundance overlap with the lower value reported by Ding et al. (2018), suggesting that the mantle source of CE-5 basalts likely has a lower S abundance than the mantle source of the Apollo 12 low-Ti basalts. Due to the similar δ^{34}S values of the CE-5 mantle source compared with that of Apollo low-Ti basalts (Liu et al., 2022; Ni et al., 2019; Wang et al.,

2024b; Wing and Farquhar, 2015), the former may originate from the same mantle source as the latter. The higher estimated S abundance in the mantle of Apollo low-Ti basalt, which might overlap with the terrestrial upper mantle (Fig. 8), compared to that of CE-5 mantle source, is consistent with continuous or intermittent extraction of volatile (e.g., S) by lunar mantle melting for > 1 billion years, which has also been suggested by a previous study on water abundance in CE-5 basalts (Hu et al., 2021). Moreover, Du et al. (2022) investigated the landing site of CE-5 mission by the radial variation of the Ti concentrations in the ejected materials around large craters and established a stratigraphic column of CE-5 landing site. Their study suggested there are 4 units of basaltic lava flows from 3.44 to 2.03 Gyrs beneath the CE-5 landing site, supporting the theory that the intermittent volcanism may cause the degassing of S.

We must emphasize that the above estimations of S abundance in the mantle of Apollo samples are based on the premise that the mantle residue was sulfide-absent. If the parental magma of the Apollo mare basalts were generally in equilibrium with high M/S ratio sulfides, then many Apollo samples' mantle residue might be sulfide-saturated, including Apollo12 low-Ti basalt (e.g., Apollo 12,008 and 12035; Brenan et al., 2019), which would result in further higher estimates of the abundance of S in the mantle, suggesting the mantle S loss would be even greater from ~ 3.2 Ga (Alexander Jr et al., 1972; Compston et al., 1971; Stettler et al., 1973) to ~ 2.0 Ga (Fig. 8). Otherwise, the extremely

low S abundance in the CE-5 mantle may also be in part be reflecting S heterogeneity in the lunar mantle.

5. Summary and Conclusions

In this study, we experimentally determined the SCSS of basaltic melts thought to be parental to young CE-5 mare basalts. We varied the experimental fO_2 and compared our results with experiments from Brenan et al. (2019). We found that for IW–2 < logfO_2 ≤ IW, the M/S ratio of sulfide increases with decreasing fO_2, and the SCSS of silicate melt decreases accordingly. Because most previous models fail to predict the SCSS of silicate melts in equilibrium with high M/S ratio sulfide under lunar-relevant fO_2, we developed a new thermodynamic SCSS model applicable to a wide range of terrestrial and lunar-relevant fO_2. With the help of our new model, we calculated the SCSS of several CE-5 parental melt candidates. The predictive SCSS values are higher than the estimated S abundances in all possible parental magmas regardless of fO_2, unless the dominant sulfide is extremely Ni-rich and S-poor, suggesting that the residual mantle source of CE-5 basalts is sulfide-absent. The reconstructed CE-5 mantle source yielded much lower S abundance (2–31 ppm) compared to the source mantle of Apollo high-Ti and low-Ti basalt, which may reflect a continuous or intermittent partial melt extraction from the lunar mantle until ~ 2 Ga, depleting the residual mantle in sulfur, or heterogeneity of lunar mantle S distribution.

CRediT authorship contribution statement

Dian Ji: Writing – review & editing, Writing – original draft, Visualization, Validation, Investigation, Formal analysis, Data curation. **Rajdeep Dasgupta:** Writing – review & editing, Supervision, Methodology, Funding acquisition, Conceptualization.

Declaration of competing interest

The authors declare that they have no known competing financial interests or personal relationships that could have appeared to influence the work reported in this paper.

Acknowledgments

Appendix A. Supplementary material

Supplementary Materials include a PDF file that describes the methods for calculating diffusion distance of S in experiments and calculation of experimental fO_2s, as well as supplementary figures, and an Excel spreadsheet with the compositions of experimental results, model calibration dataset, and new SCSS calculators. Supplementary material to this article can be found online at https://doi.org/10.1016/j.gca.2025.02.019.

Data availability

Data are available through Zenodo at https://doi.org/10.5281/zenodo.14915948.

References

Alexander Jr, E., Davis, P., Reynolds, J., 1972. Rare-gas analyses on neutron irradiated Apollo 12 samples. Lunar Science Conference.

Berthet, S., Malavergne, V., Righter, K., 2009. Melting of the Indarch meteorite (EH4 chondrite) at 1GPa and variable oxygen fugacity: Implications for early planetary differentiation processes. Geochim. Cosmochim. Acta 73 (20), 6402–6420.

Blanchard, I., Abeykoon, S., Frost, D.J., Rubie, D.C., 2021. Sulfur content at sulfide saturation of peridotitic melt at upper mantle conditions. Am. Mineral. 106 (11), 1835–1843.

Boujibar, A., Andrault, D., Bouhifd, M.A., Bolfan-Casanova, N., Devidal, J.-L., Trcera, N., 2014. Metal–silicate partitioning of sulphur, new experimental and thermodynamic constraints on planetary accretion. Earth Planet. Sci. Lett. 391, 42–54.

Brenan, J.M., 2008. Re–Os fractionation by sulfide melt–silicate melt partitioning: A new spin. Chem. Geol. 248 (3), 140–165.

Brenan, J.M., Mungall, J.E., Bennett, N.R., 2019. Abundance of highly siderophile elements in lunar basalts controlled by iron sulfide melt. Nat. Geosci. 12 (9), 701–706.

Buono, A.S., Walker, D., 2011. The Fe-rich liquidus in the Fe–FeS system from 1 bar to 10 GPa. Geochim. Cosmochim. Acta 75 (8), 2072–2087.

Callegaro, S., Geraki, K., Marzoli, A., De Min, A., Maneta, V., Baker, D.R., 2020. The quintet completed: The partitioning of sulfur between nominally volatile-free minerals and silicate melts. American Mineralogist: Journal of Earth and Planetary Materials 105 (5), 697–707.

Canup, R.M., Asphaug, E., 2001. Origin of the Moon in a giant impact near the end of the Earth's formation. Nature 412 (6848), 708–712.

Chabot, N.L., Wollack, E.A., Klima, R.L., Minitti, M.E., 2014. Experimental constraints on Mercury's core composition. Earth Planet. Sci. Lett. 390, 199–208.

Che, X., Nemchin, A., Liu, D., Long, T., Wang, C., Norman, M.D., Joy, K.H., Tartese, R., Head, J., Jolliff, B., 2021. Age and composition of young basalts on the Moon, measured from samples returned by Chang'e-5. Science 374 (6569), 887–890.

Compston, W., Berry, H., Vernon, M., Chappell, B., Kaye, M., 1971. Rubidium-strontium chronology and chemistry of lunar material from the Ocean of Storms. Proceedings of the Lunar Science Conference 2, 1471.

Danyushevsky, L.V., Plechov, P., 2011. Petrolog3: Integrated software for modeling crystallization processes. Geochem. Geophys. Geosyst. 12 (7).

Dasgupta, R., Chowdhury, P., Eguchi, J., Sun, C., Saha, S., 2022. Volatile-bearing partial melts in the lithospheric and sub-lithospheric mantle on Earth and other rocky planets. Rev. Mineral. Geochem. 87 (1), 575–606.

Day, J.M., 2018. Geochemical constraints on residual metal and sulfide in the sources of lunar mare basalts. Am. Mineral. 103 (11), 1734–1740.

Ding, S., Dasgupta, R., 2017. The fate of sulfide during decompression melting of peridotite–implications for sulfur inventory of the MORB-source depleted upper mantle. Earth Planet. Sci. Lett. 459, 183–195.

Ding, S., Dasgupta, R., Tsuno, K., 2014. Sulfur concentration of martian basalts at sulfide saturation at high pressures and temperatures – Implications for deep sulfur cycle on Mars. Geochim. Cosmochim. Acta 131, 227–246.

Ding, S., Hough, T., Dasgupta, R., 2018. New high pressure experiments on sulfide saturation of high-FeO* basalts with variable TiO2 contents–Implications for the sulfur inventory of the lunar interior. Geochim. Cosmochim. Acta 222, 319–339.

Du, J., Fa, W., Gong, S., Liu, Y., Qiao, L., Tai, Y., Zhang, F., Zou, Y., 2022. Thicknesses of Mare Basalts in the Chang'E-5 Landing Region: Implications for the Late-Stage Volcanism on the Moon. J. Geophys. Res: Planets 127 (8), e2022JE007314.

Fortin, M.-A., Riddle, J., Desjardins-Langlais, Y., Baker, D.R., 2015. The effect of water on the sulfur concentration at sulfide saturation (SCSS) in natural melts. Geochim. Cosmochim. Acta 160, 100–116.

Gaetani, G.A., Grove, T.L., 1997. Partitioning of moderately siderophile elements among olivine, silicate melt, and sulfide melt: Constraints on core formation in the Earth and Mars. Geochim. Cosmochim. Acta 61 (9), 1829–1846.

Grewal, D.S., Dasgupta, R., Sun, C., Tsuno, K., Costin, G., 2019. Delivery of carbon, nitrogen, and sulfur to the silicate Earth by a giant impact. Sci. Adv. 5 (1), eaau3669.

Grove, T.L., Krawczynski, M.J., 2009. Lunar mare volcanism: where did the magmas come from? Elements 5 (1), 29–34.

Hartmann, W.K., Davis, D.R., 1975. Satellite-sized planetesimals and lunar origin. Icarus 24 (4), 504–515.

Haughton, D.R., Roeder, P.L., Skinner, B.J., 1974. Solubility of sulfur in mafic magmas. Econ. Geol. 69 (4), 451–467.

Haupt, C., Renggli, C., Klaver, M., Steenstra, E., Berndt, J., Rohrbach, A., Klemme, S., 2023. Experimental and petrological investigations into the origin of the lunar Chang'e 5 basalts. Icarus 402, 115625.

Hauri, E.H., Saal, A.E., Rutherford, M.J., Van Orman, J.A., 2015. Water in the Moon's interior: Truth and consequences. Earth Planet. Sci. Lett. 409, 252–264.

Hauri, E.H., Weinreich, T., Saal, A.E., Rutherford, M.C., Van Orman, J.A., 2011. High pre-eruptive water contents preserved in lunar melt inclusions. Science 333 (6039), 213–215.

Holzheid, A., Grove, T.L., 2002. Sulfur saturation limits in silicate melts and their implications for core formation scenarios for terrestrial planets. Am. Mineral. 87 (2–3), 227–237.

Holzheid, A., Lodders, K., 2001. Solubility of copper in silicate melts as function of oxygen and sulfur fugacities, temperature, and silicate composition. Geochim. Cosmochim. Acta 65 (12), 1933–1951.

Hu, S., He, H., Ji, J., Lin, Y., Hui, H., Anand, M., Tartèse, R., Yan, Y., Hao, J., Li, R., 2021. A dry lunar mantle reservoir for young mare basalts of Chang'e-5. Nature 600 (7887), 49–53.

Ji, D., Dygert, N., 2023. Trace element evidence for serial processing of the lunar flotation crust and a depleted bulk Moon. Earth Planet. Sci. Lett. 602, 117958.

Johnson, A., Dasgupta, R., Costin, G., Tsuno, K., 2024. Electron Probe Microanalysis of Trace Sulfur in Basaltic Glasses and Silicate Minerals. American. Mineralogist.

Jugo, P.J., Luth, R.W., Richards, J.P., 2005. An experimental study of the sulfur content in basaltic melts saturated with immiscible sulfide or sulfate liquids at 1300 C and 1·0 GPa. J. Petrol. 46 (4), 783–798.

Kiseeva, E.S., Wood, B.J., 2013. A simple model for chalcophile element partitioning between sulphide and silicate liquids with geochemical applications. Earth Planet. Sci. Lett. 383, 68–81.

Kiseeva, E.S., Wood, B.J., 2015. The effects of composition and temperature on chalcophile and lithophile element partitioning into magmatic sulphides. Earth Planet. Sci. Lett. 424, 280–294.

Li, H., Wang, Z., Chen, Z., Tian, W., Wang, W.-R.-Z., Zhang, G., Zhang, L., 2024. A petrogenetic study of apatite in Chang'E-5 basalt: Implications for high sulfur contents in lunar apatite and volatile estimations for the lunar mantle. Geochim. Cosmochim. Acta.

Li, J., Agee, C.B., 1996. Geochemistry of mantle–core differentiation at high pressure. Nature 381 (6584), 686–689.

Li, Q.-L., Zhou, Q., Liu, Y., Xiao, Z., Lin, Y., Li, J.-H., Ma, H.-X., Tang, G.-Q., Guo, S., Tang, X., 2021. Two-billion-year-old volcanism on the Moon from Chang'e-5 basalts. Nature 600 (7887), 54–58.

Li, Y., Audétat, A., 2012. Partitioning of V, Mn, Co, Ni, Cu, Zn, As, Mo, Ag, Sn, Sb, W, Au, Pb, and Bi between sulfide phases and hydrous basanite melt at upper mantle conditions. Earth Planet. Sci. Lett. 355, 327–340.

Liu, K., Zhang, L., Guo, X., Ni, H., 2021. Effects of sulfide composition and melt H2O on sulfur content at sulfide saturation in basaltic melts. Chem. Geol. 559, 119913.

Liu, X., Hao, J., Li, R.Y., He, Y., Tian, H.C., Hu, S., Li, J., Gu, L., Yang, W., Lin, Y., 2022. Sulfur Isotopic Fractionation of the Youngest Chang'e-5 Basalts: Constraints on the Magma Degassing and Geochemical Features of the Mantle Source. Geophys. Res. Lett. 49 (15), e2022GL099922.

Liu, Y., Samaha, N.-T., Baker, D.R., 2007. Sulfur concentration at sulfide saturation (SCSS) in magmatic silicate melts. Geochim. Cosmochim. Acta 71 (7), 1783–1799.

Luo, B., Wang, Z., Song, J., Qian, Y., He, Q., Li, Y., Head, J.W., Moynier, F., Xiao, L., Becker, H., 2023. The magmatic architecture and evolution of the Chang'e-5 lunar basalts. Nat. Geosci. 16 (4), 301–308.

Malavergne, V., Cordier, P., Righter, K., Brunet, F., Zanda, B., Addad, A., Smith, T., Bureau, H., Surblé, S., Raepsaet, C., Charon, E., Hewins, R.H., 2014. How Mercury can be the most reduced terrestrial planet and still store iron in its mantle. Earth Planet. Sci. Lett. 394, 186–197.

Mavrogenes, J.A., O'Neill, H.S.C., 1999. The relative effects of pressure, temperature and oxygen fugacity on the solubility of sulfide in mafic magmas. Geochim. Cosmochim. Acta 63 (7), 1173–1180.

McDonough, W.F., Sun, S.-S., 1995. The composition of the Earth. Chem. Geol. 120 (3–4), 223–253.

Namur, O., Charlier, B., Holtz, F., Cartier, C., McCammon, C., 2016a. Sulfur solubility in reduced mafic silicate melts: Implications for the speciation and distribution of sulfur on Mercury. Earth Planet. Sci. Lett. 448, 102–114.

Namur, O., Collinet, M., Charlier, B., Grove, T.L., Holtz, F., McCammon, C., 2016b. Melting processes and mantle sources of lavas on Mercury. Earth Planet. Sci. Lett. 439, 117–128.

Ni, P., Zhang, Y., Chen, S., Gagnon, J., 2019. A melt inclusion study on volatile abundances in the lunar mantle. Geochim. Cosmochim. Acta 249, 17–41.

O'Neill, H.S.C., 2021. The thermodynamic controls on sulfide saturation in silicate melts with application to ocean floor basalts. Magma Redox Geochemistry 177–213.

O'Neill, H.S.C., Mavrogenes, J.A., 2002. The sulfide capacity and the sulfur content at sulfide saturation of silicate melts at 1400 C and 1 bar. J. Petrol. 43 (6), 1049–1087.

Papike, J., Burger, P., Shearer, C., Sutton, S., Newville, M., Choi, Y., Lanzirotti, A., 2011. Sulfides from martian and lunar basalts: Comparative chemistry for Ni, Co, Cu, and Se. Am. Mineral. 96 (5–6), 932–935.

Peach, C., Mathez, E., 1993. Sulfide melt-silicate melt distribution coefficients for nickel and iron and implications for the distribution of other chalcophile elements. Geochim. Cosmochim. Acta 57 (13), 3013–3021.

Righter, K., Pando, K., Danielson, L., 2009. Experimental evidence for sulfur-rich martian magmas: Implications for volcanism and surficial sulfur sources. Earth Planet. Sci. Lett. 288 (1–2), 235–243.

Ringwood, A., Kesson, S., 1977. Basaltic magmatism and the bulk composition of the moon: II. Siderophile and Volatile Elements in Moon, Earth and Chondrites: Implications for Lunar Origin. The. Moon 16 (4), 425–464.

Ripley, E.M., Brophy, J.G., Li, C., 2002. Copper solubility in a basaltic melt and sulfide liquid/silicate melt partition coefficients of Cu and Fe. Geochim. Cosmochim. Acta 66 (15), 2791–2800.

Saal, A.E., Hauri, E.H., 2021. Large sulfur isotope fractionation in lunar volcanic glasses reveals the magmatic differentiation and degassing of the Moon. Sci. Adv. 7 (9), eabe4641.

Smythe, D.J., Wood, B.J., Kiseeva, E.S., 2017. The S content of silicate melts at sulfide saturation: new experiments and a model incorporating the effects of sulfide composition. Am. Mineral. 102 (4), 795–803.

Steenstra, E., Berndt, J., Klemme, S., Rohrbach, A., Bullock, E., Van Westrenen, W., 2020a. An experimental assessment of the potential of sulfide saturation of the source regions of eucrites and angrites: Implications for asteroidal models of core formation, late accretion and volatile element depletions. Geochim. Cosmochim. Acta 269, 39–62.

Steenstra, E., Berndt, J., Klemme, S., Snape, J., Bullock, E., van Westrenen, W., 2020b. The fate of sulfur and chalcophile elements during crystallization of the lunar magma ocean. J. Geophys. Res. Planets 125 (11), e2019JE006328.

Steenstra, E., Seegers, A., Eising, J., Tomassen, B., Webers, F., Berndt, J., Klemme, S., Matveev, S., van Westrenen, W., 2018. Evidence for a sulfur-undersaturated lunar interior from the solubility of sulfur in lunar melts and sulfide-silicate partitioning of siderophile elements. Geochim. Cosmochim. Acta 231, 130–156.

Stettler, A., Eberhardt, P., Geiss, J., Grögler, N., Maurer, P., 1973. Ar39-Ar40 ages and Ar37-Ar38 exposure ages of lunar rocks. Proceedings of the Lunar Science Conference 4, 1865.

Su, B., Yuan, J., Chen, Y., Yang, W., Mitchell, R.N., Hui, H., Wang, H., Tian, H., Li, X.-H., Wu, F.-Y., 2022. Fusible mantle cumulates trigger young mare volcanism on the Cooling Moon. Sci. Adv. 8 (42), eabn2103.

Su, B., Zhang, D., Chen, Y., Yang, W., Mao, Q., Li, X.-H., Wu, F.-Y., 2023. Low Ni and Co olivine in Chang'E-5 basalts reveals the origin of the young volcanism on the Moon. Science Bulletin 68 (17), 1918–1927.

Su, X., Zhang, Y., 2024. Volatiles in melt inclusions from lunar mare basalts: Bridging the gap in the H2O/Ce ratio between melt Inclusions in lunar pyroclastic sample 74220 and other mare samples. Geochim. Cosmochim. Acta 373, 232–244.

Taylor, L.A., Williams, K.L., 1973. Cu-Fe-S phases in lunar rocks. American Mineralogist: Journal of Earth and Planetary Materials 58 (9–10), 952–954.

Taylor, S.R., Pieters, C.M., MacPherson, G.J., 2006. Earth-Moon system, planetary science, and lessons learned. Rev. Mineral. Geochem. 60, 657.

Thompson Jr, J., 1967. Thermodynamic properties of simple solutions. Researches in Geochemistry 340–361.

Tian, H.-C., Wang, H., Chen, Y., Yang, W., Zhou, Q., Zhang, C., Lin, H.-L., Huang, C., Wu, S.-T., Jia, L., 2021. Non-KREEP origin for Chang'e-5 basalts in the Procellarum KREEP Terrane. Nature 600 (7887), 59–63.

Tsuno, K., Dasgupta, R., 2011. Melting phase relation of nominally anhydrous, carbonated pelitic-eclogite at 2.5–3.0 GPa and deep cycling of sedimentary carbon. Contrib. Mineral. Petrol. 161, 743–763.

Tsuno, K., Grewal, D.S., Dasgupta, R., 2018. Core-mantle fractionation of carbon in Earth and Mars: The effects of sulfur. Geochim. Cosmochim. Acta 238, 477–495.

Vander Kaaden, K.E., McCubbin, F.M., 2016. The origin of boninites on Mercury: An experimental study of the northern volcanic plains lavas. Geochim. Cosmochim. Acta 173, 246–263.

Wadhwa, M., 2008. Redox conditions on small bodies, the Moon and Mars. Rev. Mineral. Geochem. 68 (1), 493–510.

Wang, C., Xu, Y.-G., Zhang, L., Chen, Z., Xia, X., Lin, M., Guo, F., 2024a. A shallow (<100 km) ilmenite-bearing pyroxenitic source for young lunar volcanism. Earth Planet. Sci. Lett. 639, 118770.

Wang, Z., Becker, H., 2013. Ratios of S, Se and Te in the silicate Earth require a volatile-rich late veneer. Nature 499 (7458), 328–331.

Wang, Z., Li, Y., Zhang, W., He, Q., Pan, F., Hu, Z., Zong, K., Feng, Y., Becker, H., Day, J. M.D., Song, W., Hui, H., Moynier, F., Jiang, Y., Zhang, X., She, Z., Wu, X., Xiao, L., Wang, L., 2024b. Sulfide compositions of young Chang'e-5 basalts and implications for sulfur isotopes in lunar basalt sources. Geochim. Cosmochim. Acta.

Wang, Z., Wang, W., Tian, W., Li, H., Qian, Y., Pei, J., Chen, Z., Wang, D., Liu, P.-P., Fa, W., Wu, J., Bao, H., 2023. Cooling rate of clinopyroxene reveals the thickness and effusion volume of Chang'E-5 basaltic flow units. Icarus 394, 115406.

Wing, B.A., Farquhar, J., 2015. Sulfur isotope homogeneity of lunar mare basalts. Geochim. Cosmochim. Acta 170, 266–280.

Wohlers, A., Wood, B.J., 2015. A Mercury-like component of early Earth yields uranium in the core and high mantle 142Nd. Nature 520 (7547), 337–340.

Wood, B.J., Fraser, D.G., 1977. Elementary thermodynamics for geologists. (no Title).

Wood, B.J., Kiseeva, E.S., 2015. Trace element partitioning into sulfide: How lithophile elements become chalcophile and vice versa. Am. Mineral. 100 (11–12), 2371–2379.

Wykes, J.L., O'Neill, H.S.C., Mavrogenes, J.A., 2015. The effect of FeO on the sulfur content at sulfide saturation (SCSS) and the selenium content at selenide saturation of silicate melts. J. Petrol. 56 (7), 1407–1424.

Zhang, H., Yang, W., Zhang, D., Tian, H., Ruan, R., Hu, S., Chen, Y., Hui, H., Lin, Y., Mitchell, R.N., Zhang, D., Wu, S., Jia, L., Gu, L., Lin, Y., Li, X., Wu, F., 2024. Long-term reduced lunar mantle revealed by Chang'e-5 basalt. Nat. Commun. 15 (1), 8328.